The MaNGA FIREFLY value added catalogue: resolved stellar populations of 10 010 nearby galaxies

Justus Neumann [1]★ Daniel Thomas [1,2] Claudia Maraston,[1] Lewis Hill [1] Lorenza Nanni,[1] Oliver Wenman,[1] Jianhui Lian [3] Johan Comparat,[4] Violeta Gonzalez-Perez [5,6] Kyle B. Westfall,[7] Renbin Yan [8] Yanping Chen,[9] Guy S. Stringfellow [10] Matthew A. Bershady,[11,12,13] Joel R. Brownstein [14] Niv Drory[15] and Donald P. Schneider[16,17]

[1]*Institute of Cosmology and Gravitation, University of Portsmouth, Burnaby Road, Portsmouth PO1 3FX, UK*
[2]*School of Mathematics and Physics, University of Portsmouth, Lion Gate Building, Portsmouth PO1 3HF, UK*
[3]*Max-Planck-Institut für Astronomie, Königstuhl 17, D-69117 Heidelberg, Germany*
[4]*Max-Planck-Institut für Extraterrestrische Physik (MPE), Giessenbachstrasse 1, D-85748 Garching bei München, Germany*
[5]*Departamento de Física Teórica, Módulo 15, Facultad de Ciencias, Universidad Autónoma de Madrid, E-28049 Madrid, Spain*
[6]*Centro de Investigación Avanzada en Física Fundamental, Facultad de Ciencias, Universidad Autónoma de Madrid, E-28049 Madrid, Spain*
[7]*University of California Observatories, University of California, Santa Cruz, 1156 High Street, Santa Cruz, CA 95064, USA*
[8]*Department of Physics, The Chinese University of Hong Kong, Shatin, N.T., Hong Kong SAR, China*
[9]*New York University Abu Dhabi, Abu Dhabi, PO Box 129188, UAE*
[10]*Center for Astrophysics and Space Astronomy, Department of Astrophysical and Planetary Sciences, University of Colorado, 389 UCB, Boulder, CO 80309-0389, USA*
[11]*South African Astronomical Observatory, PO Box 9, Observa- tory 7935, Cape Town, South Africa*
[12]*Department of Astronomy, University of Cape Town, Private Bag X3, Rondebosch 7701, South Africa*
[13]*Department of Astronomy, University of Wisconsin-Madison, 475 N. Charter Street, Madison, WI 53706, USA*
[14]*Department of Physics and Astronomy, University of Utah, Salt Lake City, UT 84112, USA*
[15]*Department of Astronomy, University of Texas at Austin, Austin, TX 78712, USA*
[16]*Department of Astronomy and Astrophysics, The Pennsylvania State University, University Park, PA 16802, USA*
[17]*Institute for Gravitation and the Cosmos, Pennsylvania State University, University Park, PA 16802, USA*

ABSTRACT

We present the Mapping Nearby Galaxies at Apache Point Observatory survey (MaNGA) FIREFLY Value Added Cata-logue (VAC) – a catalogue of ∼3.7 million spatially resolved stellar population properties across 10 010 nearby galaxies from the final data release of the MaNGA survey. The full spectral fitting code FIREFLY is employed to derive parameters such as stellar ages, metallicities, stellar and remnant masses, star formation histories, star formation rates, and dust attenuation. In addition to Voronoi-binned measurements, our VAC also provides global properties, such as central values and radial gradients. Two variants of the VAC are available: presenting the results from fits using the M11-MILES and the novel MaStar stellar population models. MaStar allows to constrain the fit over the whole MaNGA wavelength range, extends the age-metallicity parameter space, and uses empirical spectra from the same instrument as MaNGA. The fits employing MaStar models find, on average, slightly younger ages, higher mass-weighted metallicities, and smaller colour excesses. These differences are reduced when matching the wavelength range and converging template grids. We further report that FIREFLY stellar masses are systematically lower by ∼0.3 dex than masses from the MaNGA PCA and Pipe3D VACs, but match masses from the NSA best with only ∼0.1-dex difference. Finally, we show that FIREFLY stellar ages correlate with spectral index age indicators $H\delta_A$ and $D_n(4000)$, though with a clear additional metallicity dependence.

Key words: catalogues – galaxies: abundances – galaxies: evolution – galaxies: formation – galaxies: statistics – galaxies: stellar content.

1 INTRODUCTION

Stellar populations are one of the most important fossil records of galaxy evolution. They provide information about mass assembly and chemical enrichment histories including not only the integrated star formation and internal recycling processes but also pristine gas inflows, metal-loss in outflows, or mass and metal accretion through minor mergers. Observations and detailed studies of stellar populations are indispensable to constrain evolutionary processes included in models and cosmological simulations.

★ E-mail: jusneuma.astro@gmail.com

Single stars in galaxies outside the Local Group cannot (yet) be resolved and, thus, analyses depend on observations of integrated light. It has become a common approach to approximate the sum of all stellar light in one resolution element by a combination of single-age, single-metallicity stellar populations. Models of these single stellar populations (SSPs) are synthesized from stellar libraries together with stellar evolution theory in the form of an initial mass function (IMF), stellar tracks and/or isochrones (Bruzual & Charlot 1993; Worthey 1994; Vazdekis et al. 1996; Fioc & Rocca-Volmerange 1997; Maraston 1998; Leitherer et al. 1999; Bruzual & Charlot 2003; Maraston 2005; Conroy, Gunn & White 2009; Maraston & Strömbäck 2011; Maraston et al. 2020). The adopted library can be either fully theoretical (Maraston 1998), fully empirical (Vazdekis et al. 2010, 2016; Maraston et al. 2020), or a combination of both (Leitherer et al. 1999; Maraston 2005; Walcher et al. 2009; Maraston & Strömbäck 2011; Conroy et al. 2018). Complex stellar populations are then obtained by combining SSPs with arbitrary star formation histories.

In order to derive stellar population properties of data, stellar population models need to be matched to observed spectra. Over the last decades a variety of codes have been developed to perform full spectral fitting of observed spectra with varying focus on emission lines, stellar kinematics, stellar population, or all-in-one approaches: e.g. PPXF (Cappellari & Emsellem 2004; Cappellari 2017), STARLIGHT (Cid Fernandes et al. 2005), STECKMAP (Ocvirk et al. 2006a,b), GANDALF (Falcón-Barroso et al. 2006; Sarzi et al. 2006), VESPA (Tojeiro et al. 2007), ULYSS (Koleva et al. 2009) PYPARADISE (Walcher et al. 2015; Husemann et al. 2016), BEAGLE (Chevallard & Charlot 2016), FADO (Gomes & Papaderos 2017), FIREFLY (Wilkinson et al. 2017), BAGPIPES (Carnall et al. 2018), and PROSPOECTOR (Johnson et al. 2021).

With the advent of large-scale integral field unit (IFU) surveys, such as SAURON (de Zeeuw et al. 2002, 48 galaxies), ATLAS[3D] (Cappellari et al. 2011, 260 galaxies), CALIFA (Sánchez et al. 2012, 667 galaxies), SAMI (Croom et al. 2012; Bryant et al. 2015, 3068 galaxies), KMOS[3D] (Wisnioski et al. 2015, 739 galaxies), and MaNGA (Bundy et al. 2015, 10 010 galaxies), a massive amount of data has been produced for hundreds to thousands of galaxies each including thousands of spectra. Consequently, spectral fitting pipelines have been created to automatize and facilitate the process of creating 2D maps of physical galaxy parameters from observations in form of 3D datacubes (e.g. PIPE3D, Sánchez et al. 2016b; PYPIPE3D, Lacerda et al. 2022, LZIFU, Ho et al. 2016; GIST, Bittner et al. 2019; the MaNGA data analysis pipeline, DAP, Westfall et al. 2019).

The Mapping Nearby Galaxies at Apache Point Observatory survey (MaNGA; Bundy et al. 2015), a Sloan Digital Sky Survey-IV project (SDSS-IV; Blanton et al. 2017), is the largest IFU galaxy survey to date. The final MaNGA data release (SDSS-DR17; Abdurro'uf et al. 2021) contains observations of 10 010 galaxies. MaNGA data are a massive resource for studies of galaxy evolution in the nearby universe.

In this paper, we present the MaNGA FIREFLY Value Added Catalogue (VAC): a catalogue of spatially resolved stellar population parameters for all MaNGA galaxies. The pipeline to create the VAC is built upon the DAP and uses its output for further processing. The data products contained in the VAC are complementary to the high-level output of the DAP, which includes stellar kinematics, absorption-line indices, and emission-line measurements, detailed in Section 2.3. Earlier version of the MaNGA FIREFLY VAC have been described and used in Goddard et al. (2017) and Parikh et al. (2018). Here, we present the first dedicated VAC paper based on the final MaNGA data release and providing a full description and detailed

analysis of its content. This version of the VAC has already been used for scientific analysis in Neumann et al. (2021) to investigate the drivers of stellar metallicity in galaxies, showing the scientific potential of this large stellar population data base.

We describe the input and the pre-processing of MaNGA data in Section 2, the workflow to produce the VAC and details about the FIREFLY routine are presented in Section 3. Data products are shown, tested, discussed in Section 4, and compared to other catalogues in 6. We conclude in Section 7.

Throughout the paper we adopt a flat ΛCDM cosmology with a Hubble constant of $H_0 = 67.8 \,\mathrm{km\,s^{-1}\,Mpc^{-1}}$ and $\Omega_m = 0.308$ (Planck Collaboration XIII 2016).

The MaNGA FIREFLY VAC can be downloaded as FITS file from the SDSS website https://www.sdss.org/dr17/manga/manga-data/manga-firefly-value-added-catalog or from the ICG Portsmouth's website http://www.icg.port.ac.uk/manga-FIREFLY-vac. It is also available as CAS table on the SDSS skyserver http://skyserver.sdss.org/dr17 and integrated in MARVIN https://dr17.sdss.org/marvin (Cherinka et al. 2019). Examples of 2D maps of fitted stellar population parameter available in the VAC are presented in Fig. 1.

2 INPUT

The MaNGA FIREFLY VAC is a catalogue of spatially resolved stellar population parameters for MaNGA galaxies and, as such, is based entirely on observation of the MaNGA galaxy survey. We employ the full spectral fitting code FIREFLY (Wilkinson et al. 2017) to fit linear combinations of stellar population models to the observed, reduced, and pre-analysed MaNGA spectra. Hence, the two sources of input for the MaNGA FIREFLY VAC are the MaNGA data, on the one hand, and the stellar population model libraries, on the other hand.

2.1 MaNGA data

The sample of galaxies for this catalogue is drawn from the 17th and final data release[1] (DR17; Abdurro'uf et al. 2021) of the Mapping Nearby Galaxies at Apache Point Observatory survey (MaNGA; Bundy et al. 2015), a Sloan Digital Sky Survey-IV project (SDSS-IV Blanton et al. 2017). MaNGA uses IFUs that consist of 17 fibre bundles of hexagonal shape ranging from 19 to 127 fibres per bundle in order to ensure a uniform spatial coverage per galaxy (Drory et al. 2015). The IFU fibre bundles are plugged on to observation plates and feed into the BOSS Spectrographs (Smee et al. 2013) mounted at the Sloan Foundation 2.5-m Telescope (Gunn et al. 2006).

Each MaNGA plate is observed following a three-point dithering pattern to fill the inter-fibre regions and obtain uniform spatial coverage. The observations are repeated for a total observation time of $\sim$2–3 h until the S/N per pixel goal[2] is reached (Yan et al. 2016b). Each of the two spectrographs has a red and blue camera with overlapping wavelength range and a total coverage of 3622–$10\,354$Å at a median spectral resolution of $\sigma = 72 \,\mathrm{km\,s^{-1}}$. The median spatial resolution is 2.54-arcsec full width at half-maximum (FWHM), which corresponds to 1.8 kpc at the median redshift of $z \sim 0.037$ (Law et al. 2016).

The main MaNGA sample consists of a Primary sample ($\sim$ 50 per cent), a Colour-Enhanced supplement ($\sim$ 17 per cent), and

---

[1]https://www.sdss.org/dr17.
[2]The goal is to have a continuum S/N of 33 per pixel in the *r*-band stacked between $1R_e$ and $1.5R_e$.
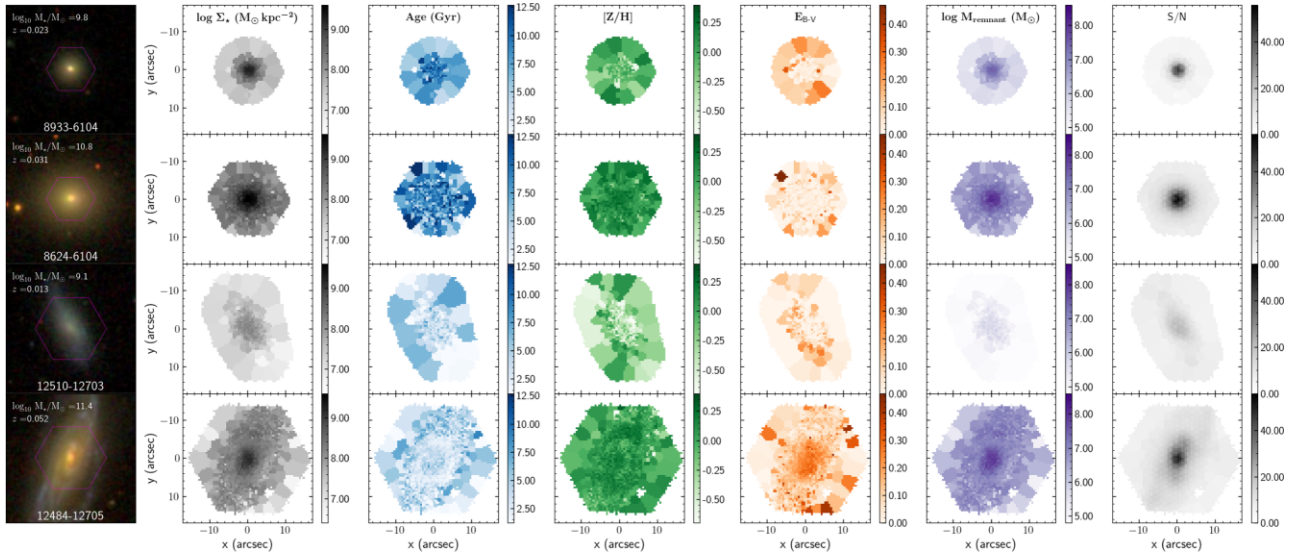
Figure 1. Example 2D maps from the `FF-Mi` variant of the MaNGA FIREFLY VAC showing different stellar population parameters, dust attenuation, and signal-to-noise ratios (S/N).

a higher redshift Secondary sample (~ 33 per cent). The main selection criteria is a flat stellar mass distribution $M_\star > 10^9\,M_\odot$ in logarithmic space with a uniform spatial coverage out to $1.5R_e$ for the Primary sample and $2.5R_e$ for the Secondary sample, where R_e is the effective radius of a given galaxy. The Colour-Enhanced supplement fills poorly sampled regions in the colour–magnitude diagram (Law et al. 2015; Wake et al. 2017) and it covers out to $1.5R_e$. In addition to the main sample, the full catalogue also includes observations from ancillary programmes,[3] which make about ~ 5 per cent of the total sample and are processed by FIREFLY, as well. These include single galaxy observations as well as mosaicing of larger regions from a variety of science programmes.

Observations have been concluded in 2020 August and the final sample has been released in Abdurro'uf et al. (2021). The total number of datacubes is 11 273 including 10 145 galaxy observations of high quality corresponding to 10010 unique galaxies. The MaNGA FIREFLY VAC provides the stellar populations for 10 735 of these datacubes.[4]

All raw data are processed by two survey pipelines: the MaNGA data reduction pipeline (DRP; Law et al. 2016) and the MaNGA data analysis pipeline (DAP; Westfall et al. 2019) to provide high-level science-ready data products, which are essential inputs for the FIREFLY VAC project.

2.2 Data reduction pipeline

The main task of the DRP is to read the raw data from MaNGA observations and extract, calibrate and combine them into FITS files that are ready for scientific analysis. This is a sophisticated multistep process that is described in full detail in Law et al. (2016) and updates to DR15 in Aguado et al. (2019) and to DR17 in Abdurro'uf et al. (2021). In addition, the detailed modelling of the line-spread function

(LSF) is described in Law et al. (2021). Here, we provide only a very short summary.

First, the flux of each fibre is extracted, flatfielded, and wavelength calibrated using specific calibration frames. The background sky is then determined from a combination of eight dedicated sky fibres and subtracted from each of the science fibre spectra. Afterwards, each spectrum is flux calibrated employing standard star observations from 12 small seven-fibre bundles with the same fibre size and fill-factor as the science fibre bundles (Yan et al. 2016a). The two spectra from the blue and red camera are then combined into a single spectrum and resampled on to a common wavelength array. The output of the first stage is a FITS file containing row-stacked spectra (RSS) of one fully reduced spectrum per fibre. During the second stage, the astrometry of each exposure is registered and the series of 2D RSS are combined and resampled into a 3D datacube with a grid of 0.5 arcsec per pixel. The DRP produces one datacube for each 'PLATEIFU'[5] designation.

2.3 Data analysis pipeline

Every datacube that has been produced by the DRP and that has an initial redshift estimate is fed into the DAP for the analysis of higher level data products. In addition to the DRP datacubes as input, the DAP uses photometric measurements of the ellipticity and position angle of the target from the parent catalogue (Wake et al. 2017); the enhanced NASA Sloan Atlas.[6] For each datacube, the DAP produces spatially resolved stellar kinematics, emission-line properties, and spectral indices. In the following, we provide a short outline of the DAP workflow, full details can be found in Westfall et al. (2019) and for the emission-line fitting in Belfiore et al. (2019).

The pipeline is executed in a series of six main modules that are tasked for: DRP output assessment, spatial binning, stellar kinematics fitting, emission-line moments fitting, Gaussian emission-line modelling, and stellar index measurement. The assessment stage secures

---

[3] https://www.sdss.org/dr17/manga/manga-target-selection/ancillary-targets/.
[4] The MaNGA FIREFLY VAC processes all datacubes that successfully run through the DAP. From the total number of 11 273 datacubes, 538 failed during the DAP run due to various reasons.

[5] Each MaNGA target is identified by its own 'MaNGA-ID', but some targets are observed multiple times. 'PLATEIFU' is a string with a unique plate-IFU combination for a given observation.
[6] M. Blanton; www.nsatlas.org.

that a spectrum is only analysed if 80 per cent of the data points are valid and, in addition, it computes the *g*-band weighted S/N per spectrum. This is followed by spatial Voronoi binning (Cappellari & Copin 2003) of the spectra to a minimum target S/N ∼ 10 per bin. Afterwards, all fitting modules are executed multiple times using different combinations of binned and unbinned data, the name of each approach is saved in the keyword 'DAPTYPE'. For DR17, the DAP provides output products for analysis of single spaxels ('SPX'), of Voronoi-binned spectra ('VOR10'), and of a hybrid binning scheme, where the stellar continuum is fitted on the binned spectra while the emission lines are measured per spaxel ('HYB10'). Similar to the fitting of stellar kinematics, stellar population analysis usually requires higher S/N in the continuum than emission-line analysis due to the much stronger signal in the emission lines. The MaNGA FIREFLY VAC therefore uses exclusively the 'VOR10' DAP output.

The stellar kinematics are fitted employing the penalized pixel-fitting method (pPXF; Cappellari & Emsellem 2004; Cappellari 2017) with a hierarchically clustered selection of stellar templates from the MILES library (Sánchez-Blázquez et al. 2006), providing a higher spectral resolution. For the stellar continuum modelling in the emission-line module, the DAP uses a different library: With the advantage of full wavelength coverage, in DR17, a subset of the MaStar SSP library (Maraston et al. 2020) is used. The last stage is the measurement of stellar indices on the emission-line subtracted spectra. These include absorption line indices and bandhead indices.

The two main output products are a 'MAPS' file, which contains 2D maps of high-level data products, and a 'LOGCUBE' file, which contains the original and best-fitting model spectra as well as emission-line spectra for each DRP datacube (observation/'PLATEIFU'). In addition, there is a single summary 'DAPall' catalogue that provides global galaxy properties.

The main source of input to the MaNGA FIREFLY VAC are the DAP data products. In particular, the MaNGA FIREFLY VAC uses for each datacube per Voronoi bin: coordinates, *g*-band S/N, velocity, velocity dispersion (from MAPS file), observed spectrum, emission-line spectrum, bitmask, inverse variance, line spread function (from LOGCUBE file), and redshift (from DAPall file).

2.4 Stellar population model libraries

The current version of the MaNGA FIREFLY VAC released together with SDSS DR17 is offered in two structurally identical variants with the only difference being the stellar population model library employed to fit the observed spectra. Both models are based on the same stellar evolution (as in Maraston 2005) and IMF assumption and the difference between them is the adopted stellar spectral library.

The first variant uses the M11-MILES model templates from Maraston & Strömbäck (2011) as in the previous versions of the VAC. These single-burst stellar population models are based on the MILES stellar library (Sánchez-Blázquez et al. 2006) and inherit its native wavelength coverage, from 3500 to 7430 Å, and spectral resolution of 2.54 Å FWHM (Beifiori et al. 2011; Falcón-Barroso et al. 2011). The population synthesis code adopts isochrones and stellar tracks by Cassisi, Castellani & Castellani (1997) for ages older than 30 Myr and by Schaller et al. (1992) for younger ages. Here, we use the models that are based on a Kroupa (2001) IMF. The parameter grid of the M11-MILES models ranges between 50 ages from 6.5 Myr to 15 Gyr and 10 metallicities [Z/H] from −2.25 to 0.35. At [Z/H] = −1.3 and −2.3, the age coverage is limited to > 2 and > 5 Gyr, respectively (due to the stellar age distribution of the input library). The exact grid coverage is shown in Fig. 2.
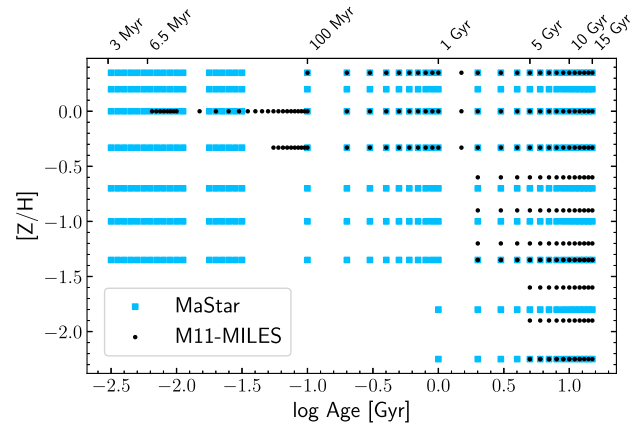

Figure 2. Age-metallicity grid of the two stellar population libraries used in the VAC.

The second variant uses an updated version of the MaStar SSP models described in Maraston et al. (2020), which are based on the MaStar stellar library (Yan et al. 2019). One of the main advantages to use the MaStar SSPs for fitting MaNGA data is that the empirical spectra are taken with the exact same instrument, hence, they match the galaxy observations in wavelength coverage (3600 – 10 300 Å) and resolution (*R* = 1400–2200). The models are based on the same population synthesis code and input physics as M11-MILES (Maraston & Strömbäck 2011), described in detail in Maraston (2005). For the DR17 version of the MaNGA FIREFLY VAC we employ version 1.1 of the models – dubbed 'gold' – which are based on the nineth MaStar Product Launch (MPL-9) of the MaStar stellar library.[7] These models use a combination of the stellar parameters derived by Hill et al. (2022), Chen et al. (2020), and Lazarz et al. (in preparation). The 'gold' version used here represents the best-performing ones among them, according to the calibration criteria described in Maraston et al. (2020). The gold MPL-9 model library includes templates down to 3 Myr. The full grid covers ages from 3 Myr to 15 Gyr and metallicities [Z/H] from −2.25 to 0.35. We note that the current MaStar version does not include yet the thermally pulsating asymptotic giant branch (TP-AGB) contribution to the stellar evolution. The MaStar population models using MPL-11 and the further set of parameters by Imig et al. (2022) will be published in Maraston et al. (in preparation). In addition to age and metallicity, a third parameter of the MaStar template grid allows for a flexible low-mass IMF slope from *s* = 0.3 to 3.8. We adopt here a Kroupa (2001) IMF with slope *s* = 1.3 for consistency with the other model variant and previous studies, and leave the IMF analysis to future papers. As can be seen in Fig. 2, the parameter coverage of MaStar is much improved as compared to M11-MILES, thanks to the significantly larger sample size of the MaStar stellar library, which extends to hotter temperatures leading to a larger parameter range in models. To summarize, the full wavelength range, the same instrument, and the excellent parameter coverage make the MaStar SSPs a very suitable library to fit MaNGA observations.

3 WORKFLOW

The main task to construct the MaNGA FIREFLY VAC is full spectral fitting of Voronoi-binned MaNGA data. This is the first out of two steps and it is executed employing the FIREFLY code for each binned
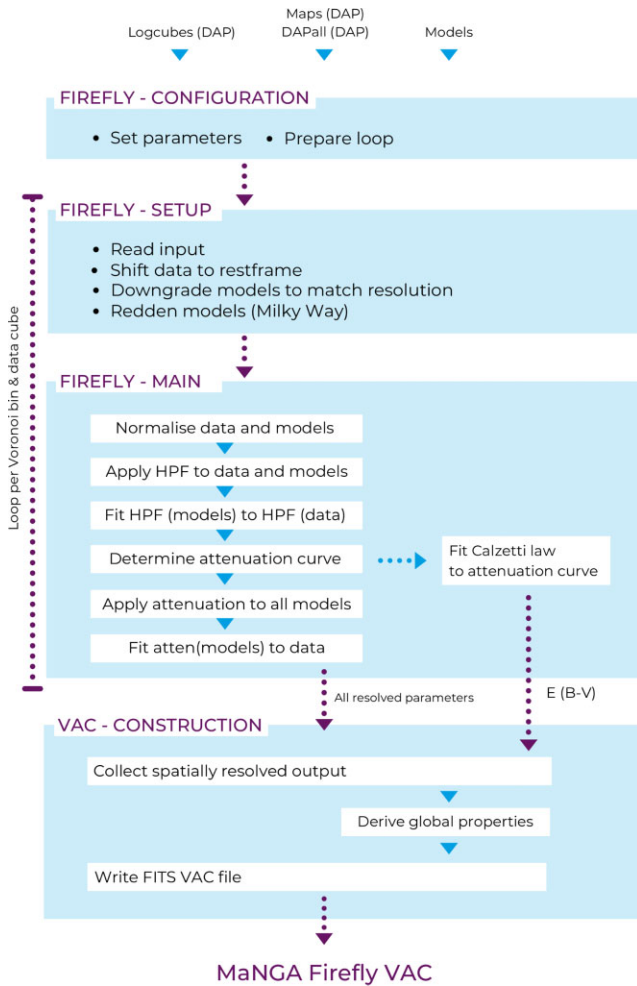
---

[7]http://www.icg.port.ac.uk/mastar.

Figure 3. Workflow. Details are described in Section 3.

spectrum in each datacubes separately, in other words, ∼3.7 million times in total. The second step is performed by a single PYTHON script that collects all output, calculates global galaxy parameters, and produces the final VAC file.

In the following, we first give a short general summary of FIREFLY, then, we present the specific setup and the run used for this catalogue, and, lastly, we describe the final construction of the VAC. The workflow is summarized in Fig. 3.

3.1 FIREFLY: code

FIREFLY[8] (Wilkinson et al. 2017) is a full spectral fitting code written in PYTHON designed to obtain properties of stellar populations from spectral integrated light observations. It compares arbitrarily weighted linear combinations of single-burst models to the observed spectrum and aims at iteratively minimizing χ^2 controlled by the Bayesian information criterion. All solutions within a statistical cut are retained, which allows to obtain uncertainty intervals based on the likelihood distribution of fitting solutions.

The code was written with low S/N surveys, such as BOSS (Eisenstein et al. 2011; Dawson et al. 2013) and MaNGA (Bundy et al. 2015), in mind and was shown to perform well down to S/N∼5

Table 1. FIREFLY configuration for the DR17 VAC.

	FF-Mi	FF-Ma
Models	m11-MILES	MaStar-gold
IMF	Kroupa	Kroupa
Age limits	< 'AoU' (z)	< 'AoU' (z)
Z limits	None	None
Dust law	Calzetti + 2000	Calzetti + 2000
Em-line masking	Off	Off

Notes. FF-Mi and FF-Ma refer to the two variants of the DR17 MaNGA FIREFLY VAC employing the m11-MILES and the MaStar-gold model libraries, respectively (see Section 2.4). 'AoU'(z) means the age of the universe at the respective redshift. Calzetti + 2000 refers to the dust law presented in Calzetti et al. (2000).

(figs 8–16 in Wilkinson et al. 2017). One of the main concepts is to allow for a large fitting freedom and sufficient exploration of the parameter space. As such, neither additive nor multiplicative polynomials are employed and star formation histories are not regularized. A novel method is used to account for dust attenuation, in which a high-pass filter (HPF) is applied to the spectrum to isolate small-scale features, such as absorption lines, from large-scale variations, such as dust attenuation but also inaccurate flux calibration. For more detail about the code as well as extensive performance tests, we refer to Wilkinson et al. (2017). Further applications and testing of performance are presented in Goddard et al. (2017) and Comparat et al. (2017).

3.1.1 Updates of FIREFLY v1.0.1

A new version of FIREFLY has been released together with the MaNGA FIREFLY VAC: version 1.0.1. The update includes: (a) a major revision of the interface, (b) user-level changes/bug fixes, and (c) fixes and changes to the DR17-specific MaNGA setup. A more detailed list can be found on the GITHUB webpage,[9] here we would like to point out a few essentials: A cap on the maximum number of fit objects to be created per iteration is removed, as in some cases it generated a bias in templates files used. MaStar and M11-MILES-SG SSPs are added. The MaNGA datacube-specific LSF (Law et al. 2021) is used instead of a generic averaged MaNGA resolution. Functionality of emission-line masking and masking of individual pixels is improved.

3.2 FIREFLY: configuration/setup

The FIREFLY configuration file contains a small number of important user-level parameters such as the stellar population library to be used, the IMF, limits on age and metallicity to constrain the library, whether or not to mask emission lines and which lines to mask, as well as which dust law to use to calculate the colour excess $E(B - V)$. In addition, it includes some further technical parameters. The configuration of the DR17 VAC is presented in Table 1.

The setup procedure prepares the input data (from MAPS, LOGCUBE and DAPall) before the main FIREFLY run can be executed. This is done for each spectrum separately and, thus, it is part of the loop over all Voronoi-binned spectra from all DAP datacubes. First, the observed spectrum and the emission-line spectrum is read and the latter subtracted from the former. The bitmask and inverse variance arrays are passed on to FIREFLY. Secondly, redshift and

relative stellar velocity are used to shift the emission-line-subtracted spectrum to rest-frame wavelengths. Thirdly, all model templates are downgraded by matching the intrinsic model resolution to the LSF and stellar velocity dispersion. Furthermore, all models are reddened (Fitzpatrick 1999) to match the line-of-sight Milky Way reddening of the observations using the coordinates of the source and the maps of Schlegel, Finkbeiner & Davis (1998).

3.3 FIREFLY: run

The main steps of the FIREFLY fitting procedure are outlined in Fig. 3; a slightly more detailed version of this part of the workflow is shown in Wilkinson et al. (2017, fig. 3).

(1) The observed spectrum and all model templates are normalized to the total integrated flux. The normalization factors are saved and will be used later to convert light-weights to mass-weights. (2) An HPF is applied to both data and models to remove long wavelength modes. (3) A weighted linear combination of the filtered model templates are fitted to the filtered data. (4a) The attenuation curve is determined as

$$F_{\mathrm{Atte}}(\lambda) = \frac{F_{\mathrm{data}}(\lambda)}{F_{\mathrm{bestfit}}(\lambda)} - \frac{\mathrm{HPF}(F_{\mathrm{data}}(\lambda))}{\mathrm{HPF}(F_{\mathrm{bestfit}}(\lambda))}. \tag{1}$$

In the first term of that equation, $F_{\mathrm{data}}(\lambda)$ is the unfiltered data spectrum and $F_{\mathrm{bestfit}}(\lambda)$ is the reconstructed full best-fitting model combination. The ratio between both is the sum of the large-scale variations (i.e. the attenuation curve) and the residuals of the fit. The latter must therefore be subtracted to obtain $F_{\mathrm{Atte}}(\lambda)$. Subsequently, the attenuation curve is smoothed. (4b) In a parallel step, the attenuation curve is fitted with the Calzetti et al. (2000) law to obtain the colour excess E_{B-V} (shown on the right-hand side of Fig. 3). (5) The smooth attenuation curve (not the Calzetti-fitted curve) is applied to all unfiltered model templates. (6) The unfiltered data are fitted in a second fitting cycle with a weighted linear combination of the reddened unfiltered model templates. All solutions within a statistical cut are retained to construct the likelihood distribution. The best fit is the peak of the distribution and the confidence intervals for each stellar population parameter are obtained within the corresponding likelihood intervals (see fig. 7 in Wilkinson et al. 2017).

The output of the FIREFLY run consists of the observed input spectrum, the associated error spectrum, the best-fitting model spectrum, and a series of stellar population parameters: the full SFH with light-weights and mass-weights of the individual SSPs, light- and mass-weighted average age and metallicity defined as

$$\langle \mathcal{P} \rangle_{\mathrm{LW}} = \sum_{i=1}^{n} w_i^{\mathrm{L}} \mathcal{P}_i, \qquad \langle \mathcal{P} \rangle_{\mathrm{MW}} = \sum_{i=1}^{n} w_i^{\mathrm{M}} \mathcal{P}_i, \tag{2}$$

where $\mathcal{P}$ is either age or Z, w_i^{L} is the light-weight, and w_i^{M} the mass-weight of the ith SSP. Note that these parameters are linearly averaged. Further outputs are the colour excess $E(B-V)$, the total stellar mass and its partition into masses of living stars, white dwarfs, neutron stars, black holes, and stellar ejecta. The division of mass is obtained by applying mass-loss factors on the mass of each SSP contribution that depend on age, metallicity, and IMF. The adopted initial mass-final mass theoretical relations are described in Maraston (1998, 2005) and are based on Renzini & Ciotti (1993). Two examples of a fit with FIREFLY to the emission-line-subtracted stellar continuum of the central spaxel are shown in Figs 4 and 5, for a relatively young population with strong emission lines and for a quiescent old population, respectively. The figure also exemplifies the slightly different results obtained according to the choice of the model library.

3.4 VAC construction

After fitting all individual spectra of all datacubes with FIREFLY, the VAC construction PYTHON script is executed. The main purpose of this script is to (1) collect all output from FIREFLY, (2) derive global stellar population properties (see next subsections), and (3) write everything in a single FITS file. The only spatially resolved property, in addition to the FIREFLY output, that is computed as part of this script is the stellar surface mass density, which is derived as

$$\Sigma_{\star,i} = M_{\star,i} / A_i, \tag{3}$$

where $M_{\star,i}$ is the stellar mass and A_i is the projected[10] surface area of the ith Voronoi bin in any given galaxy.

3.4.1 Central values and values at $1R_e$

In addition to spatially resolved stellar population measurements, as part of the MaNGA FIREFLY VAC, we also provide global galaxy properties, specifically, characteristic values such as the average age and metallicity in the galaxy centre, at $1R_e$, and gradients within $1.5R_e$.

We measure the central average stellar population properties within a fixed circular aperture of 3-arcsec diameter. The motivation of this choice is to provide a direct comparison from the IFU observations of MaNGA galaxies to large SDSS catalogues from single 3-arcsec-fibre spectroscopy. The obvious caveat is that these measurements are not sensitive to inclination and distance effects. In case the user of this VAC is interested in central values that are averaged over a more similar physical space in each galaxy, we advise to derive those from the spatially resolved measurements in an elliptical aperture of flexible size.

In contrast to the central values, we employ elliptical apertures for the derivation of the characteristic values at the effective radius. In particular, the value at the effective radius is averaged within two concentric ellipses at $0.9R_e$ and $1.1R_e$, while having the angle of the semi-major axis aligned with the position angle of the galaxy.

It is important to point out that we do not rebin and reanalyse the spectra but, in fact, we average the results from the Voronoi-binned FIREFLY analysis. In detail, the average of the light-weighted (mass-weighted) parameters is calculated as the mean of all Voronoi bins within the aperture weighted by their relative flux (mass) contribution:

$$\langle \mathcal{P} \rangle_{\mathrm{LW}} = \frac{\sum_{i=1}^{n} \mathcal{P}_{\mathrm{LW},i} f_i a_i}{\sum_{i=1}^{n} f_i a_i}, \qquad \langle \mathcal{P} \rangle_{\mathrm{MW}} = \frac{\sum_{i=1}^{n} \mathcal{P}_{\mathrm{MW},i} m_i a_i}{\sum_{i=1}^{n} m_i a_i},$$

where n is the total number of Voronoi bins within the aperture. For the ith Voronoi bin, $\mathcal{P}_i$ is the measured parameter, f_i is the g-band-weighted mean flux, m_i is the stellar mass as returned by FIREFLY, and a_i is the fraction of the bin area that is inside the aperture. These values are always computed as long as the number of included Voronoi bins is non-zero. Errors are calculated from the weighted average upper and lower error boundaries of the $\mathcal{P}_i$. Light- and mass-weighted age and metallicity within the central 3 arcsec and at $1R_e$ are provided in the FITS extension HDU2.

3.4.2 Gradients within $1.5R_e$

Similar to the average value at the effective radius, we also derive the radial gradients of each galaxy in elliptical coordinates (i.e. taking

---

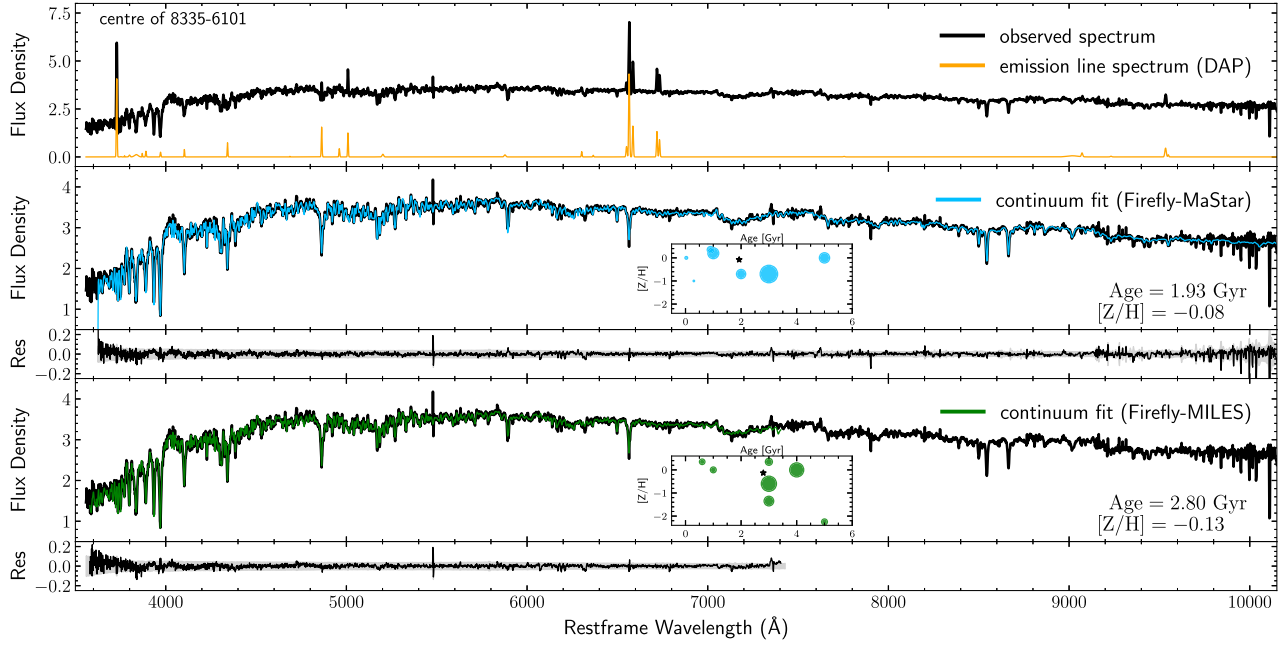[10]We do not apply an inclination correction.

Figure 4. Example spectrum and modelling from the central spaxel of PLATEIFU = 8335-6101 ($z = 0.018$). Top panel: observed spectrum and emission-line spectrum as derived by the DAP. Middle panel: emission-line subtracted spectrum and stellar continuum fit by FIREFLY using the `MaStar` SSPs. Residuals of the fit are shown below the spectrum. The grey shaded area shows the uncertainty on the observation. Inset plot shows the star formation history, i.e. the age-metallicity grid of SSPs used to fit the spectrum. The size of the dots corresponds to the mass fraction contributed to the total population. Mean age and metallicities are shown as star symbols and are annotated in the bottom right-hand panel. Bottom panel: same as the middle panel but employing the `M11-MILES` SSPs.

Figure 5. Same as Fig. 4 but for a spectrum from the central spaxel of PLATEIFU = 8257-12704 ($z = 0.025$) showing no emission lines and an old stellar population. Grey-shaded wavelength regions are masked during fitting.

into account the inclination), but within a larger aperture of $1.5R_e$. We impose a minimum number of 10 bins within the aperture as a requirement to compute the gradient.

The gradient is calculated by first running a median along 10 equally sized radial bins and subsequently fit a linear regression to the binned median values. We estimate the statistical uncertainty of each gradient by performing 100 bootstrap realizations of the linear fit using randomly resampled bins. The light- and mass-weighted age and metallicity gradients as well as the corresponding zero-points are given in the FITS extension `HDU3`.

3.4.3 Changes compared to DR15 VAC

The major change in the MaNGA FIREFLY VAC is the addition of stellar population properties calculated with the new SDSS-IV-based MaStar set of stellar population models, covering the full wavelength range of the data. In addition, we decided to drop absorption line strength indices in DR17, which were included in SDSS DR15 and earlier versions of the VAC (cf. Goddard et al. 2017), as these are now provided by the DAP.

Further small changes to the DR15 version include that the radius in HDU4 is now given in elliptical coordinates and the azimuth is added. Masses in HDU11 and HDU12 are given per spaxel and as total mass per Voronoi cell.

3.4.4 Star formation rates

The latest addition to the MaNGA FIREFLY VAC is the derivation of spatially resolved and global star formation rates (SFRs). This has been performed after the SDSS VAC release and is, therefore, not part of the DR17 version of the VAC. We will make the full table of SFRs publicly available as separate files and as part of upcoming versions of the VAC.

SFRs are calculated directly from the derived stellar masses and ages by integrating mass fractions over a given age range. The range to be considered is somewhat arbitrary and depends on the definition of *current* SFR. For example, the last 10 Myr trace the time interval of photoionization from young, massive stars probed by the Hα recombination line, while 100 Myr is often used to calibrate star formation tracers from the far-infrared (e.g. Kennicutt 1998). We provide both measurements and define the SFR of the ith Voronoi bin as

$$\mathrm{SFR}_i = \sum_{\mathrm{SSP}_{t=0}}^{t_n} M_{\mathrm{SSP},i} \bigg/ \Delta t \, , \tag{4}$$

where M is the total mass of a certain SSP template (not corrected for mass-loss) and the sum goes over all SSP templates of age $t = 0$ to $t_n = 10$ or 100 Myr. The total SFR per galaxy is then derived as sum over all local SFRs across the galaxy FoV.

4 DATA PRODUCTS

4.1 Overview

The complete VAC is provided in a single FITS file per model variant manga-FIREFLY-v3_1_1-miles.fits and manga-FIREFLY-v3_1_1-mastar.fits of ~ 6.1-GB size and include all 16 Header-Data Units (HDUs) as detailed below. Additionally, there is a light-weight version of only global parameters manga-FIREFLY-globalprop-v3_1_1-miles.fits and manga-FIREFLY-globalprop-v3_1_1-mastar.fits of ~ 2.8-MB size containing HDU0–HDU3. All four files can be accessed from the SDSS webpage.[11]

  (i) HDU0: empty;
  (ii) HDU1: general galaxy information, pipeline versions;
  (iii) HDU2–HDU3: global galaxy stellar population properties;
  (iv) HDU4–HDU15: spatially resolved parameters.

A detailed description of the FITS file content is given in Table A1 and in the official datamodel.[12] In addition, we provide spatially resolved and global SFRs, as well as the results from fitting-performance analyses in separate files on the ICG institute's website.[13]

4.2 FF-Mi versus FF-Ma

4.2.1 Individual fits

In this section, we show the distributions of the derived parameters and at the same time compare both variants of the catalogue. In Figs 4 and 5, we illustrate how the use of different model libraries can lead to different best-fitting linear combinations of SSPs and, thus, different average quantities. In Fig. 6, we compare the spatially resolved average stellar population parameters for all fits with S/N > 5 in the VAC (~3.7 million) between the FF-Mi and the FF-Ma variants.

The best agreement is found for stellar masses, here represented as surface mass density; not surprisingly, as this is known to be typically the most robust parameter. Note, however, that different choices of IMFs, isochrones and spectral fitting codes lead to systematic offsets that we discuss in Section 6.1.

Looking at light-weighted metallicity and age, we find that metallicity agrees reasonably well with an average difference of $\Delta\mu_{[Z/H],LW} \equiv [Z/H]_{LW,Ma} - [Z/H]_{LW,Mi} = -0.03 \pm 0.09$ dex. A larger systematic difference is seen between the ages with $\Delta\mu_{Age,LW} = -0.11 \pm 0.18$. MILES-derived mean ages are on average older than MaStar-derived ages at all age bins. In particular, FF-Mi does not go younger than 1 Gyr. Maraston & Strömbäck (2011) already noted that MILES-based population models led to older ages with respect to to e.g. population models based on STELIB. Part of the reason might be intrinsic in the stellar parameters associated to the MILES library. Part of the effect, however, simply comes from the parameter coverage in that the M11-MILES library lacks low-metallicity, low-age templates. When such stellar populations occur, these absent templates are likely to be replaced by the next possible older ones leading to older ages on average. Following this scenario, we are also able to explain the higher dust attenuation derived in FF-Mi. In the first fitting loop, FIREFLY determines the best-fitting template combination based only on the small-scale variations in the spectrum. An older best-fitting SSP combination will lead to smaller fluxes when the full spectrum is compared to the data. This will subsequently be compensated for by the attenuation curve (known as age-dust degeneracy), leading to higher attenuation values in FF-Mi as compared to FF-Ma.

Light-weighted averages are dominated by the young stellar populations and it is, thus, on the one hand, not surprising that mass-weighted ages are significantly shifted towards older average ages in both variants of the VAC. The density plot draws the attention to a tail of some populations that appear old in FF-Mi but quite young for mass-weighted ages in FF-Ma. However, this is a very small fraction of the data and the majority of data points are confined to old average ages on both axes with a mean difference that remains, in fact, almost unchanged as compared to the light-weighted counterparts. The distributions of ages are in line with our current understanding that more than half of the stellar mass of galaxies has already been in

---

[11]https://data.sdss.org/sas/dr17/manga/spectro/firefly/v3_1_1.

[12]https://data.sdss.org/datamodel/files/MANGA_FIREFLY/FIREFLY_VER/manga_firefly.html.
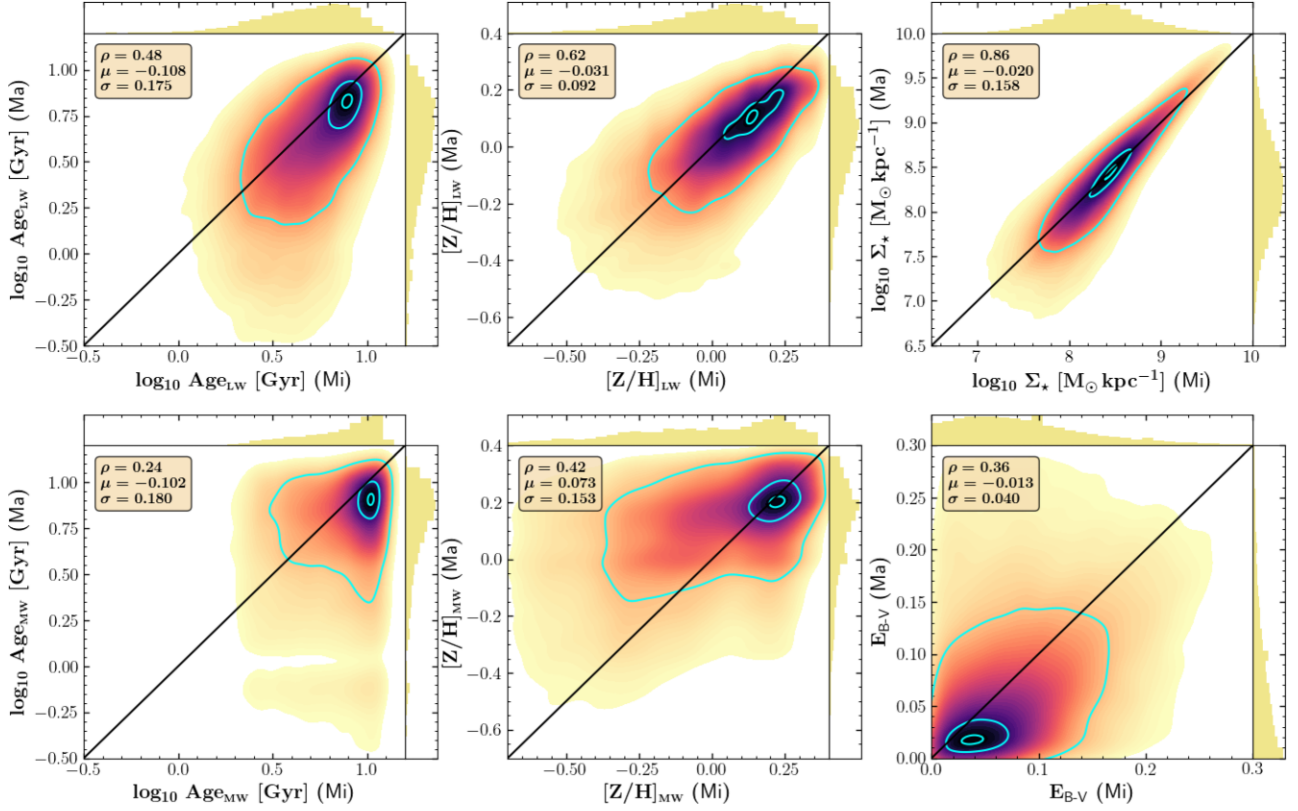[13]http://www.icg.port.ac.uk/manga-firefly-vac/.

Figure 6. Comparison of the stellar population properties of MaNGA galaxies between both VAC variants FF-Mi and FF-Ma. Density plots visualize the 2D distribution while histograms on top and to the right of each panel show the 1D distribution of each property. Colours and histograms are in linear scales where darker colours correspond to higher densities. Cyan contours enclose 1, 10, and 68 per cent of the distribution. In the top left corner, we annotate the Spearman's rank correlation coefficient ρ, the median difference $\Delta\mu$ between the parameters y and x, and the median absolute deviation σ.

place 10 Gyr ago Madau & Dickinson (2014). Explaining differences between light- and mass-weighted metallicites, on the other hand, is not straight forward. The mass-weighted metallicities in FF-Ma are on average $\Delta\mu_{[Z/H],MW} = 0.07 \pm 0.15$ dex higher than in FF-Mi. This is possibly caused by the age-metallicity degeneracy in that the older SSPs are compensated by more metal-poor SSPs. The difference is not seen in light-weighted averages and is even slightly reversed. The aforementioned compensation of young templates can happen dominantly in the old component and is even more likely to happen in the old component given the lack of young, metal-poor templates. This explains why the metallicity difference between FF-Mi and FF-Ma is only seen in the mass-weighted plot. In fact, the near-infrared extension of MaStar is able to capture more metal lines that are more relevant in the older populations and, therefore, metallicity should be better constrained in FF-Ma.

To shed further light on differences between light- and mass-weighted metallicity averages, it is informative to compare them directly. From a close-box chemical evolution scenario, one would expect younger stellar populations to be more chemically mature or in other words more metal-rich. Hence, the light-weighted average population would have a higher metallicity than the mass-weighted one. Yet, at a given age, the lower the metallicity the brighter the spectrum; a circumstance acting contrary to the effect of the age. In addition to both of that, chemical evolution of galaxies is not as simple as a closed-box scenario and inflows, outflows, feedback and mergers make these simplistic views more complex.

In Fig. 7, we directly compare mass-weighted to light-weighted metallicity for both VAC variants. Both parameters are strongly
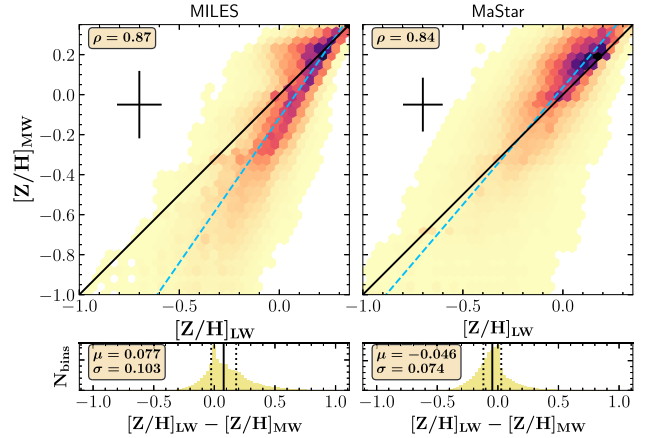

Figure 7. Comparison between light- and mass-weighted average metallicity for both VAC variants. The errorbar shows the median individual uncertainty of each measurement. A linear regression is shown as blue dashed line. The parameters ρ, μ, and σ have the same meaning as in Fig. 6.

linearly correlated. Yet, the slope of the correlation is larger than one yielding a crossing of the one-to-one line such that at low metallicities, mass-weighted values are lower while at high metallicities, light-weighted values are lower. In FF-Mi, lower mass-weighted values dominate most of the distribution, while in FF-Ma, mass-weighted values are more often higher. The differences between both variants probably arise from the covered wavelength range. In FF-
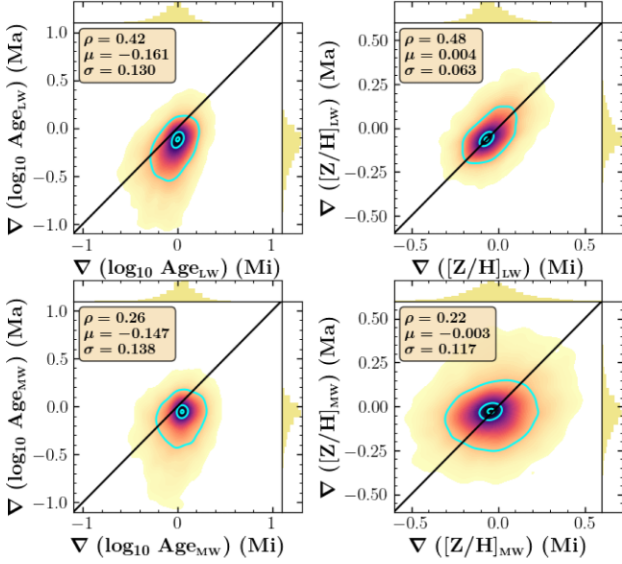
Figure 8. Comparison of linear radial age and metallicity gradients derived within $1.5R_e$ between both VAC variants. Colour scale, contours, and statistical parameters have the same meaning as in Fig. 6.

Mi, bluer wavelengths are covered, the flux of which is dominated by younger populations yielding higher light-weighted metallicities. With FF-Ma fitting redder wavelengths, this effect becomes less dominant and even slightly reversed at high metallicities.

4.2.2 Gradients

Radial gradients of gas-phase abundances or stellar populations in galaxies have been extensively studied in the literature (e.g. Sánchez-Blázquez et al. 2014; González Delgado et al. 2015; Belfiore et al. 2017; Goddard et al. 2017; Lian et al. 2018; Poetrodjojo et al. 2018; Oyarzún et al. 2019; Lacerna et al. 2020; Neumann et al. 2020, 2021). The MaNGA FIREFLY VAC calculates gradients on an individual galaxy-by-galaxy basis as described in Section 3.4.2. It is instructive to study how the individual differences between FF-Mi and FF-Ma fits affect global galaxy properties such as gradients. In Fig. 8, we present and compare the distribution of light- and mass-weighted age and metallicity gradients for both VAC variants.

Light-weighted gradients are well correlated with an excellent agreement between the metallicity gradients. Age gradients are systematically more negative in FF-Ma. This indicates that the age difference for individual fits as seen in Fig. 6 is larger at larger radii, which are often dominated by young star-forming regions. Mass-weighted gradients are very flat in both variants. Age and metallicity peak close to zero in both distributions. Age gradients are again slightly smaller in FF-Ma. The scatter in the metallicity gradient distribution is of the order of the measurement error (see e.g. Fig. 7) and likely reflects the uncertainty in determining mass-weighted gradients.

4.3 Differential effects of input parameters

To further aid our understanding of the differences between both variants of the VAC and to test the robustness of the results, in this subsection, we explore the effect of the choice of the IMF, the fitted wavelength range, the model parameter grid and emission-line masking on the derived stellar population parameters.

For these tests, we semi-randomly selected a subsample of 300 galaxies from the main MaNGA sample while monitoring that the distribution in stellar mass, colour, age, and metallicity are representative of the overall sample. In addition to both VAC variants FF-Mi and FF-Ma, we created another five mini-VACs of these 300 galaxies with varying FIREFLY configurations. The setup is shown in Table 2. Each mini-VAC contains ∼100 000 sets of spatially resolved parameters. Detailed figures comparing the fitted parameters can be found in Appendix B. Here, we discuss the main results.

4.3.1 Initial mass function

Both main variants of the VAC use stellar population models that employ the Kroupa (2001) IMF. While it is known that the choice of the IMF only affects the computed stellar mass (e.g. Pforr, Maraston & Tonini 2012), it is instructive to inspect all stellar population parameters and, at the same time to quantify the change in stellar mass. For this comparison, we use the exact same FIREFLY configuration with the MaStar model grid based on a low-mass IMF slope of 1.3 for a Kroupa IMF (FF-Ma) and a slope of 2.35 for a Salpeter (1955) IMF (config4).

Age, metallicity and dust attenuation show no systematic differences ($\Delta\mu \leq 0.01$ dex) with a scatter comparable to the average uncertainty of the measurements ($\Delta\sigma \leq 0.1$ dex). Surface mass density shows a clear systematic offset with small scatter towards higher masses when employing a Salpeter IMF. The median difference is $\Delta\mu = 0.170 \pm 0.075$ dex, in other words, models with a Salpeter IMF produce masses by a factor of 1.48 higher than models based on a Kroupa IMF in very good agreement with the theoretical factor of 1.5 reported in Maraston (2005), and slightly lower than the offset of 0.209 dex found in Pace et al. (2019a). From fitting broad-band photometry of mock galaxies over a wide wavelength range with a wide range of templates, Pforr et al. (2012, tables 3 and 4) report offsets of 0.28 for star-forming and 0.08 for quiescent galaxies at a redshift of $z = 0.5$, on average in good agreement with our result. See also Domínguez Sánchez et al. (2019), where they show that the mass-to-light ratio of MaNGA early-type galaxies is ∼1.5 times higher for the Salpeter IMF than for the Kroupa (right-hand panel of their fig. 17).

4.3.2 M11-MILES: squared grid models

One of the major differences between the MaStar SSPs and M11-MILES that we used to explain discrepancies between the VAC variants is the grid coverage, in particular the lack of low-metallicity, low-age MILES templates. We try to test the effect by employing a special 'squared-grid' version of the M11-MILES models, henceforth called M11-MILES-SG. These models use complementary high-resolution theoretical stellar population model spectra from Maraston et al. (2009) based on the Rodríguez-Merino et al. (2005) model atmospheres, then smoothed to the MILES resolution. The extended M11-MILES-SG models have been used in Trussler et al. (2020) for the analysis of DR17 SDSS integrated galaxy spectra.

When comparing the results using M11-MILES-SG (config3) with FF-Ma, we find that the addition of young model templates does produce more similar light-weighted ages among both catalogues, especially in the lower age range. That also leads to a slight improvement for the mass-weighted metallicities. Yet, a disagreement clearly remains at older average ages. We conclude that template grid coverage is an important factor when comparing stellar population

Table 2. FIREFLY setup for the configuration tests.

	FF-Mi	FF-Ma	config1	config2	config3	config4	config5
Models	M11-MILES	MaStar-gold	MaStar-gold	M11-MILES	M11-MILES-SG	MaStar-gold	MaStar-gold
IMF	Kroupa	Kroupa	Kroupa	Kroupa	Kroupa	Salpeter	Kroupa
Wavelength range	Short	Full	Full	Short	Short	Full	Short
Em-line masking	Off	Off	On	On	Off	Off	Off

parameters, but it is not sufficient to explain the differences. On the other hand, it is also important to note that while `M11-MILES-SG` has an improved squared coverage, the sampling of the grid between the libraries remains non-identical.

4.3.3 Wavelength range

Another difference between MILES and MaStar is the wavelength coverage. We explore the importance of covering the full wavelength range in MaStar (i.e. $3600-10\,300$ Å) by producing another mini-VAC using the exact same MaStar configuration except for the wavelength range that we limit to the range of the MILES library (`config5`).

The fits with the short wavelength range (i.e. 3600–7430 Å) produce indeed on average slightly older ($\Delta\mu_{\mathrm{Age,LW}} = 0.04 \pm 0.17$ dex) and more metal-poor ($\Delta\mu_{\mathrm{[Z/H],LW}} = -0.05 \pm 0.09$ dex) results, an indication that the long MaStar/MaNGA wavelength range helps to break the age-metallicity degeneracy (e.g. Maraston 2005). Comparing the short wavelength range MaStar results with MILES, we find that the average differences are reduced but remain present.

We further look at the combined effect of wavelength range and grid coverage by comparing the fits using the short MaStar models (`config5`) with those using the squared grid MILES models (`config3`). As expected, light- ($\Delta\mu_{\mathrm{Age,LW}} = -0.03 \pm 0.17$ dex) and mass-weighted age ($\Delta\mu_{\mathrm{Age,MW}} = -0.06 \pm 0.17$ dex) and metallicity ($\Delta\mu_{\mathrm{[Z/H],MW}} = 0.01 \pm 0.15$ dex) differences are reduced even further, yet remaining to a lower degree. We conclude that the differences between both main variants of our MaNGA FIREFLY VAC can be explained to a large extent by the combined effect of model template grid coverage and fitted wavelength range. The remaining discrepancies most likely lie in the assumed stellar parameters, which assign an empirical spectrum to a temperature–gravity—metallicity location of stellar evolution, investigated in detail in Maraston et al. (2020).

4.3.4 Emission-line masking

Finally, we compare fits with subtracted emission lines with fits with masked emission lines for both M11-MILES (`config2`) and MaStar models (`config1`). With both model libraries, we obtain on average slightly older and slightly more metal-rich parameters when emission lines are masked. However, differences are small ($\Delta\mu < 0.02$ dex). Since a lot of care has been taken to accurately model the emission lines in the DAP (Belfiore et al. 2019), we chose to use the emission-line subtracted spectra without masking for both variants of the MaNGA FIREFLY VAC.

4.4 Stellar remnants

In addition to stellar ages, metallicities, masses, dust attenuation, and star formation histories, the MaNGA FIREFLY VAC also contains spatially resolved information of stellar remnants. These include black holes, neutron stars and white dwarfs. The masses of the
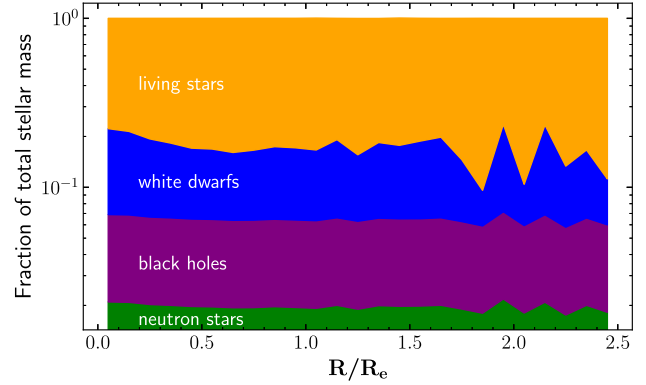

Figure 9. Average fractional contribution of stellar remnants to the total stellar mass per spatial bin as a function of radius. Due to the large parameter range, we show fractions in log units. Based on the 300 galaxy subsample introduced in Section 4.3.

remnants are derived by applying mass-loss factors to the SSPs (Maraston 2005), as described in Section 3.3. An example showing 2D maps of the total mass of stellar remnants is shown in Fig. 1.

Another instructive way to look at these quantities is shown in Fig. 9. This plot shows the fraction of stellar remnants to the total stellar mass as a function of radius. All fractions are calculated as the average of all spatial bins of the 300 galaxy test sample from the previous subsection. Interestingly, the fractional mass of all remnants is slightly radially decreasing between the centre and $R = 0.7R_{\mathrm{e}}$, most prominently seen for white dwarfs. The reason for that might be related to radially decreasing age, as younger populations contain more living stars. To test this hypothesis, we bin the galaxies in four groups of different radial light-weighted stellar age gradient intervals and show the same plot for each group of galaxies in Fig. 10. Indeed, galaxies with the steepest age gradient, have also the strongest radial decrease of remnants. Figs 9 and 10 exemplify the potential of the data contained in the VAC. Detailed maps of stellar remnants will be presented and discussed in a forthcoming paper.

5 PERFORMANCE

The MaNGA FIREFLY VAC does not explicitly provide any quality flags of the data products. On the one hand, the input data have already been subject to quality control in the processing of the DRP and DAP. Only successful DAP output was considered for further FIREFLY fitting. We strongly recommend to use the data products in combination with quality control flags as provided by the DRP and DAP. On the other hand, all output parameters in the VAC are paired with an error estimation as detailed in Section 3. In addition, in this section, we study the general quality of the fits by considering the individual spectral residuals between observations and best-fitting models. These measurements are not part of the official VAC release but will be made publicly available alongside the VAC at http://www.icg.port.ac.uk/manga-firefly-vac.
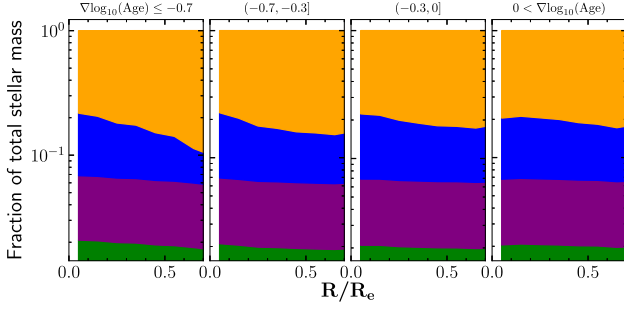
Figure 10. Same as Fig. 9 but for galaxies divided into four different bins of radial stellar age gradient. Shown are only the inner $0.7R_e$.

The procedure to characterize the goodness of the spectral fits in the MaNGA FIREFLY VAC is for the most part adapted from Westfall et al. (2019). We calculate for each fit the fractional residual per wavelength channel $\Delta_{f,i} = |f_{\mathrm{obs},i} - f_{\mathrm{model},i}|/f_{\mathrm{model},i}$ and the error-normalized residual $\Delta_{\mathcal{E},i} = |f_{\mathrm{obs},i} - f_{\mathrm{model},i}|/\mathcal{E}_i$. Here, f_i is the flux of the observed or best-fitting model spectrum at wavelength channel i, and $\mathcal{E}_i$ is the corresponding error of the observed flux. We define then the fractional root mean square fRMS and the reduced χ_ν^2 as

$$f\mathrm{RMS} = \sqrt{\frac{1}{N}\sum_{i=1}^{N}\Delta_{f,i}^2}, \qquad (5)$$

$$\chi_\nu^2 = \sum_{i=1}^{N}\Delta_{\mathcal{E},i}^2 \Big/ (N - \nu), \qquad (6)$$

where N is the total number of fitted wavelength channels and ν is the number of model templates with non-zero weight. In Fig. 11, we plot fRMS and χ_ν^2 against the g-band S/N per fit, in other words, per Voronoi bin. For a theoretically perfect fit, we expect an anticorrelation between fRMS and S/N and a constant, close-to-one χ_ν^2.

The observed trends in Fig. 11 are very similar to the ones seen for the stellar continuum fits by the DAP and are discussed in detail in Westfall et al. (2019, their fig. 27 and section 11.2.1). The fRMS follow a clear log-log anticorrelation with S/N. We observe a slight flattening in the relation at high S/N, which is paralleled by an up-bending of χ_ν^2. At these S/N, systematic errors in the modelling start to dominate random errors. Overall, the distribution of χ_ν^2 is mostly flat with a median value of $\langle\chi_\nu^2\rangle = 0.87 \pm 0.05$ for FF-Mi and $\langle\chi_\nu^2\rangle = 0.90 \pm 0.07$ for FF-Ma. The fact that χ_ν^2 is on average smaller than 1 could be a sign of overfitting, but is rather likely due to an overestimation of the flux error (cf. Westfall et al. 2019). There is no significant difference in the performance of the fits between FF-Mi and FF-Ma. The median χ_ν^2 value of FF-Ma is higher by 0.03, which is probably caused by the noisier part of the spectra at large wavelength covered by the MaStar models. In fact, when the MaStar fits are limited to the MILES wavelength range (config5), the median χ_ν^2 drops to 0.85 ± 0.05.
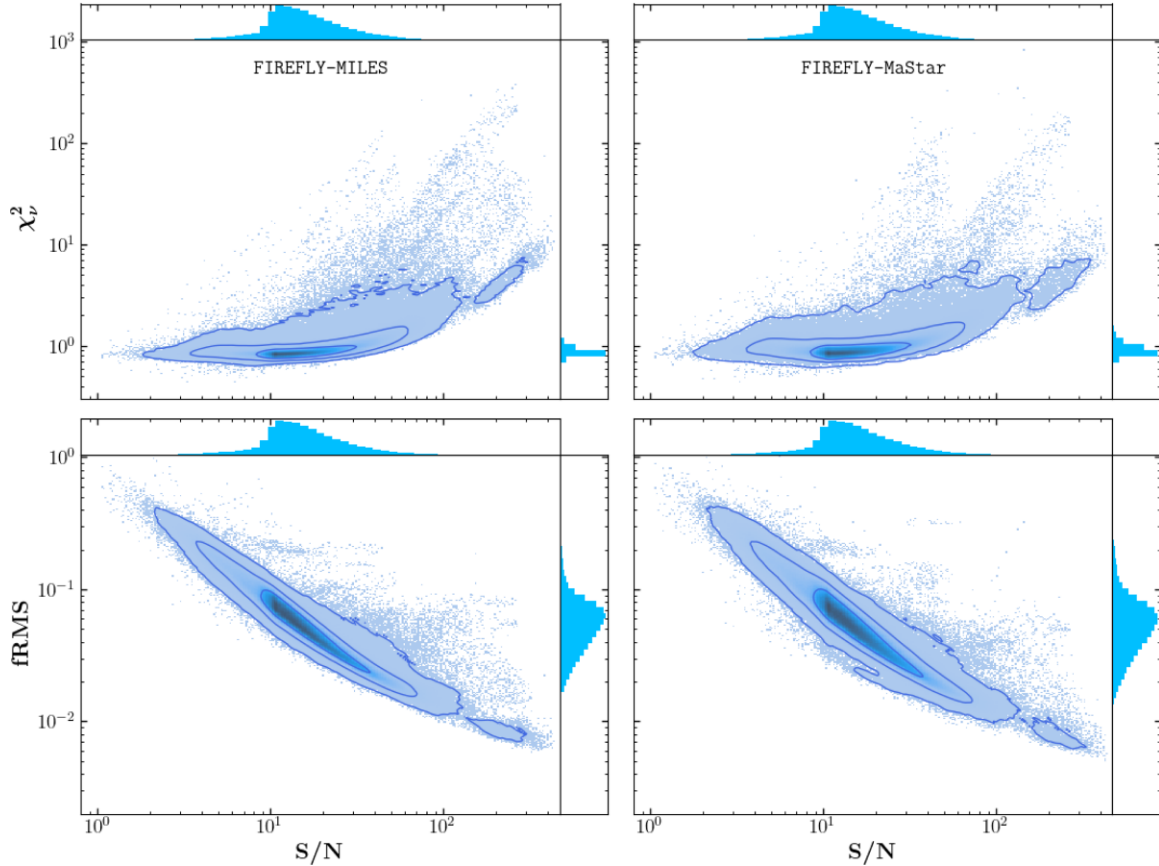

Figure 11. Goodness of FIREFLY fits to MaNGA data. Shown are the reduced χ_ν^2 as well as the root mean square of the fractional residuals fRMS as a function of g-band S/N. The complete sample of spectral fits is included. 2D densities and marginals are in linear scales with darker regions corresponding to higher densities. Contours enclose 1σ, 2σ, and 3σ of the distribution.
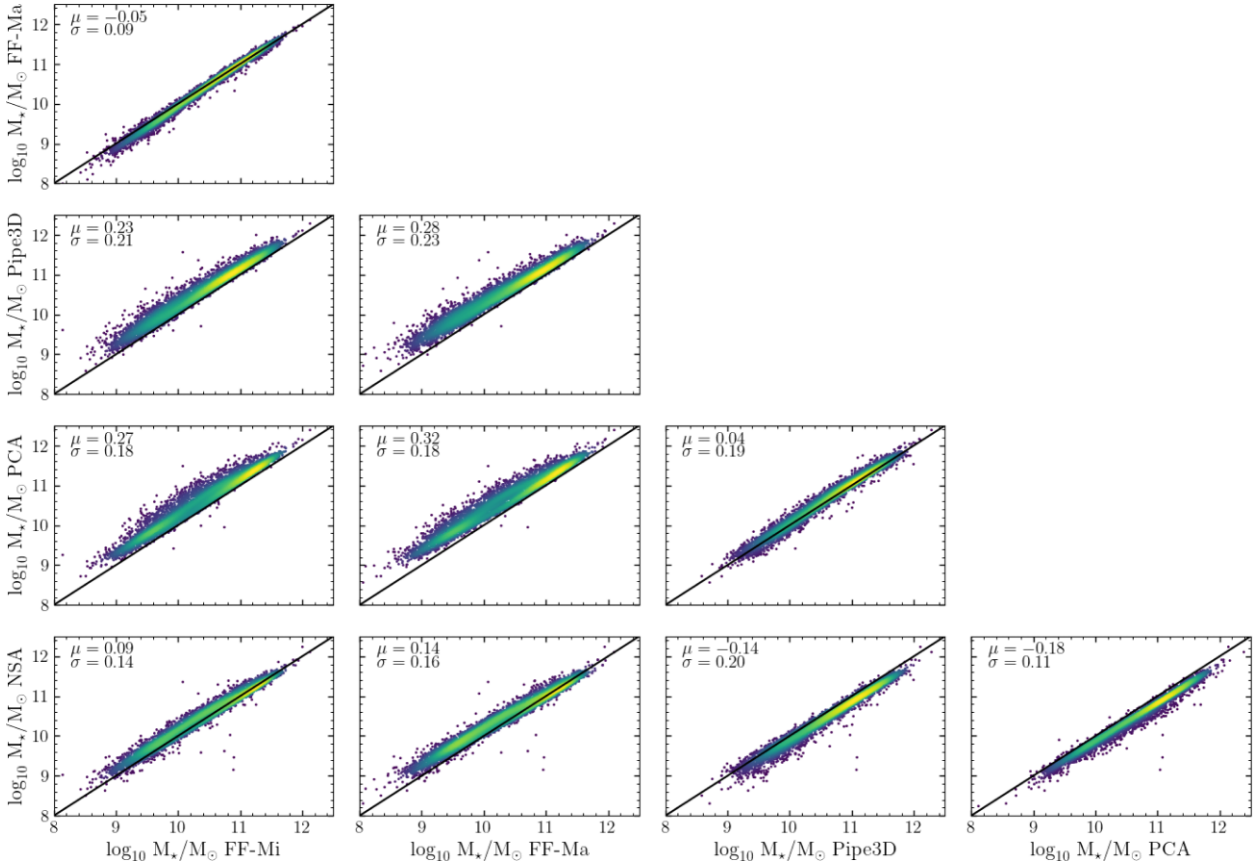
Figure 12. Total stellar masses of DR17 MaNGA galaxies as listed in different catalogues. All masses are converted into a cosmology with $H_0 = 67.8 \, \text{km s}^{-1} \, \text{Mpc}^{-1}$, Kroupa IMF, and are aperture corrected.

6 COMPARISON WITH OTHER MANGA CATALOGUES

A total number of 63 VACs have been released in SDSS as of DR17, of which 25 are updated or new in DR17 (Abdurro'uf et al. 2021). This includes three stellar population modelling VACs of MaNGA data: the Principle Component Analysis VAC (PCA; Pace et al. 2019a,b), the Pipe3D VAC (Sánchez et al., in preparation, see Sánchez et al. 2018 for earlier versions) based on the new pipeline version pyPipe3D (Lacerda et al. 2022) originally described in Sánchez et al. (2016a), and the MaNGA FIREFLY VAC. In this section, we compare some of our results with the DR17 version of these VACs and output from the DAP.

6.1 Total galaxy masses

The mass is a fundamental parameter in the characterization of a galaxy and is one of the main drivers of physical processes as part of both the dynamical and chemical evolution (e.g. Kauffmann et al. 2003; Peng et al. 2010; Thomas et al. 2010). The determination of the stellar mass through full spectral fitting with stellar population models is usually more robust to the exact combination of SSP templates than other parameters such as age or metallicity because of degeneracy effects. While there is indeed little scatter in mass between the configuration tests performed in the previous section, the absolute calibration of stellar masses depend on several assumptions, e.g. the cosmological parameters, the IMF and the input physics used in the population synthesis code.

Spatially resolved stellar masses in the MaNGA sample are available in the MaNGA FIREFLY VAC variants (1) FF-Mi and (2) FF-Ma, (3) in the PCA VAC, (4) in the Pipe3D VAC, and (5) total galaxy masses in the NASA SLoan Atlas (NSA; Blanton et al. 2011; Wake et al. 2017). For future reference when comparing MaNGA works based on stellar mass measurements from different sources, we show in Fig. 12 a cross-comparison between each of the catalogues.

A number of notes have to be made. The MaNGA VACs (1)–(4) are based on resolved IFU data, but use mutually different binning schemes. Therefore, we decided to only compare *total* galaxy masses that are additionally also comparable to the photometry-based measurement from the NSA catalogue. The total mass in (1)–(4) is simply the sum across the MaNGA field of view. All masses are converted to the cosmology used in the FIREFLY VAC, i.e. Planck Collaboration XIII (2016). Furthermore we shift all Pipe3D masses, which assume a Salpeter IMF, by 0.17 dex using the offset found in Section 4.3.1 so that all catalogues use Kroupa IMF equivalent masses. The sample in (1), (2), (4), and (5) is the DR17 sample. The comparison to (3) is based on the common DR15 subsample, since the DR17 version of the PCA VAC was not yet available at the writing of this paper. Finally, we apply an aperture correction to all IFU-based measurements, i.e. VACs (1)–(4), using the correction factors based on the *CMLR* method from Pace et al. (2019b). In this method the mass of each galaxy outside the IFU is calculated from the missing flux using colour–mass-to-light relations (Pace et al. 2019a).
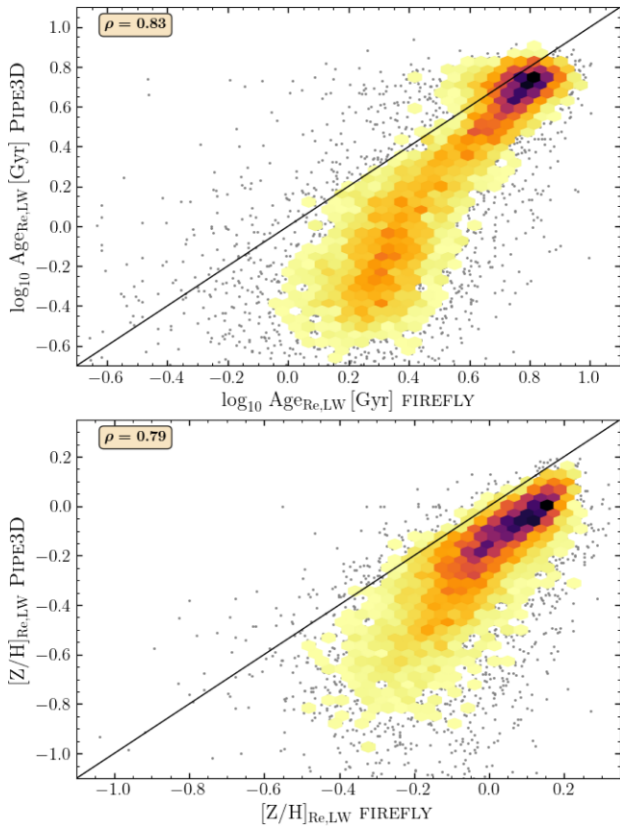
Figure 13. Comparison of light-weighted stellar ages and metallicities averaged within a ring at $1R_e$ between Pipe3D and FIREFLY (FF-Ma).

The scatter between any pair of catalogues in Fig. 12 is of the order of 0.2 dex with the exception of the two FIREFLY VACs with $\sigma = 0.09$ dex. There are clear systematic offsets between all catalogues: As compared to FF-Ma with the lowest masses, the offsets in dex are 0.05 for FF-Mi, 0.14 for NSA, 0.28 for Pipe3D, and 0.32 for PCA, which reports the highest masses. The stellar masses published in the Pipe3D VAC are masses of living stars only. The offset reported here is therefore likely to increase by ∼0.1 dex (cf. Fig. 9) if remnants are included.

Differences between these catalogues are likely due to different input libraries, stellar tracks and mass-loss prescriptions. The PCA VAC uses an unpublished theoretical stellar library and Padova 2008 (Marigo et al. 2008) isochrones to synthesize the models used in the VAC. The DR17 version of the Pipe3D VAC uses an unpublished model library based on the MaStar stellar library using a code from Bruzual & Charlot (BC19, private communication). Hence, at this point, it is difficult to pin-point the exact sources leading to the discrepancies, but the different inputs in the model libraries are the most likely reason.

6.2 Stellar ages and metallicities from Pipe3D

The Pipe3D VAC comprises an extensive catalogue of stellar populations and emission-line properties of MaNGA galaxies that are derived independently and in parallel to the properties of the DAP and the FIREFLY VAC. An in-depth comparison between both VACs is very desirable and necessary. Nevertheless, there are a few complications to overcome. Firstly, both VACs use different Voronoi binning schemes. Therefore, fitting is performed on non-identical spectra and

a direct one-to-one comparison of the stellar population properties is not possible. Instead, we will focus on averaged 'global' galaxy properties. Secondly, the comparison of star formation histories is a complex multidimensional problem and, therefore, comparisons must rely on averaged stellar populations. Pipe3D uses geometric means while the FIREFLY VAC uses arithmetic means. The geometric mean is always lower than the arithmetic mean by an amount that correlates with the variance in the data. It is beyond the scope of this paper to recalculate the means from the star formation histories. None the less, it is still instructive to look for correlation between both VACs in a qualitative way.

In Fig. 13, we compare the mean light-weighted age and metallicity at the effective radius for the complete sample of ∼10 000 galaxies between FF-Ma and Pipe3D, of which both VACs are based on the MaStar stellar library. The Pipe3D parameter is averaged between two concentric ellipses at 0.75 and $1.25R_e$, while in the MaNGA FIREFLY VAC, we average between 0.9 and $1.1R_e$. As expected, Pipe3D-derived mean ages and metallicities are systematically lower, most probably because of the usage of geometric means. However, we reiterate and note that both VACs adopt different stellar population models. The systematic difference in Fig. 13 is larger at lower values, which is likely caused by a larger spread in the star formation histories. While a comparison of the total values is therefore impeded, we find a strong monotonic correlation as attested by the Spearman's rank correlation coefficients of $\rho = 0.83$ and 0.79. We acknowledge this as encouraging indication of a good agreement.[14] Further and more detailed studies are needed to fully explore both VACs in comparison.

6.3 SFRs from Pipe3D

Local and global star formation activity is one of the main parameters used to characterize galaxies on large scales and to learn about star formation processes on sub-kpc scales. MaNGA provides the opportunity to measure both spatially resolved and global star formation of 10 010 galaxies. A variety of star formation tracers across the electromagnetic spectrum are frequently been used, most notably Hα as the strongest recombination line tracing the ionization of young, massive stars.

A full stellar population analysis as performed in this VAC offers probably the most direct probe of recent star formation by delivering a full decomposition of stellar ages. The SFR in the MaNGA FIREFLY VAC is calculated as sum over all mass of stellar populations younger than 10 and 100 Myr divided by the corresponding time interval (see Section 3.4.4). Similarly, Pipe3D provides SFR measurements averaged over 10, 32. and 100 Myr. In addition, Pipe3D also provides the SFR based on dust-corrected Hα flux measurements. As we did for the stellar age and metallicity comparison, we compare our SFRs to the Pipe3D Hα-based SFRs on a global, per-galaxy basis, since individual binning schemes differ between both VACs.

For this comparison, we only select star-forming galaxies with clear Hα detection, characterized by $|EW(H\alpha)| > 3$ Å at $1R_e$, following Sánchez et al. (in preparation). Fig. 14 shows that our SSP-based SFRs generally correlate well with Hα-based SFRs from Pipe3D. The best correlation with the lowest scatter is found for $SFR_{SSP,100\,Myr}$ in FF-Ma with an offset of $\Delta \log_{10} SFR_{SSP-H\alpha} =$

---

[14] The results of both stellar population VACs are not expected to fully agree, given the different approaches in the astrophysical modelling involved in the procedure. None the less, it is essential to explore discrepancies and congruencies.
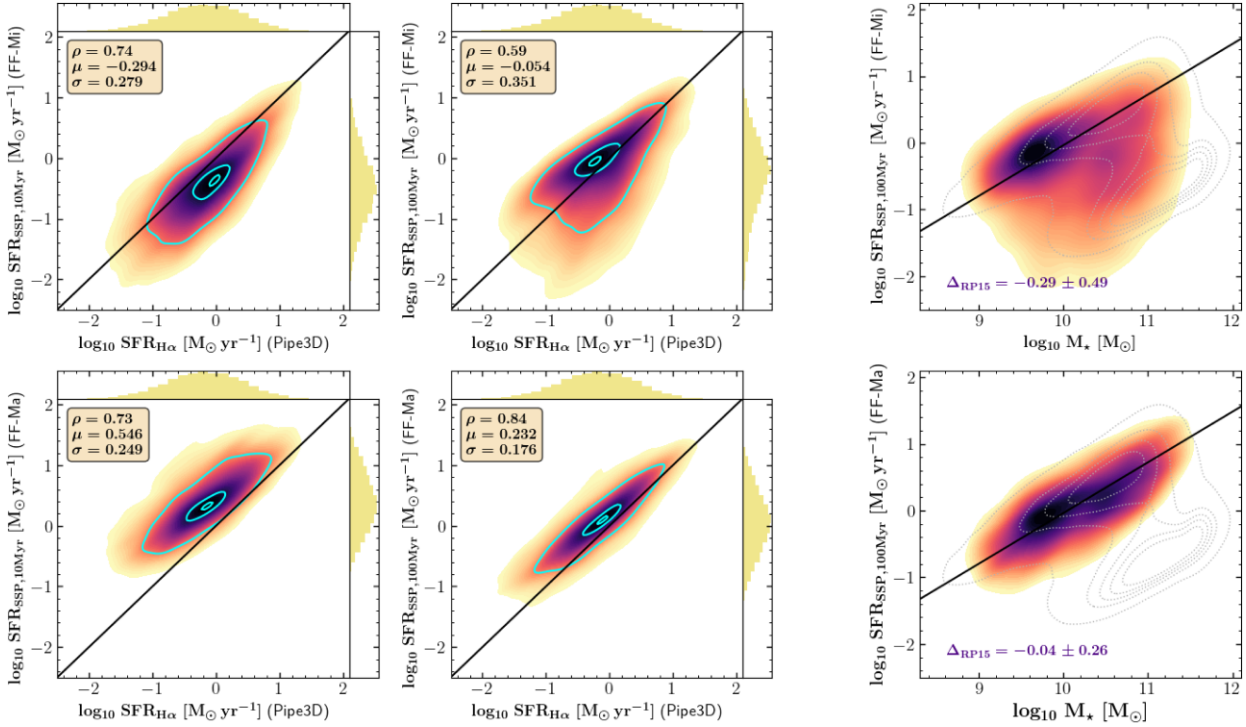
Figure 14. Left-hand and middle column: comparison of SFRs between the SSP-based approach in the MaNGA FIREFLY VAC and the Hα-based SFRs from Pipe3D. Shown are SFRs considering a 10- and 100-Myr time interval. Colours, contours, histograms, and statistical parameters are as in Fig. 6. Right-hand column: SFR–$M_\star$ plot. Colours show the density distribution of our SSP-based measurements, while grey contours indicate the distribution of SDSS galaxies (Brinchmann et al. 2004). The black solid line marks the star formation main sequence as determined in Renzini & Peng (2015). Our sample is limited to galaxies with $|EW(H\alpha)| > 3$ Å at $1R_e$.

Figure 15. Comparison between FIREFLY-derived stellar ages and metallicities with spectral indices from the DAP. Leftmost two panels: Stellar ages versus EW(Hδ) and $D_n(4000)$. Values from FF-Ma are shown in blue, FF-Mi is shown in green. Solid lines are light-weighted, dashed lines are mass-weighted median ages. Regions between the 16th and 84th percentile of light-weighted values are shown as shades. Errorbars show the median error of individual measurements. Right two panels: same as the left-hand panels, but only showing light-weighted ages separated in bins of stellar metallicity. This figure shows the results from the subsample of 300 galaxies introduced in Section 4.3.

0.232 ± 0.176. FF-Mi likely underestimates SFRs due to the lack of young SSP templates. The effect is larger for the younger (shorter) 10-Myr range. Despite the offset of FF-Ma SFRs, we find that their distribution agrees exceptionally well with the main sequence of star formation as shown in the right-hand panels, where we overplot our star-forming sample with the contours from the distribution of DR7 SDSS galaxies based on Brinchmann et al. (2004). The median difference to the main sequence as parametrized in Renzini & Peng (2015) is $\Delta_{RP15} = -0.04 \pm 0.26$.

6.4 Spectral indices and dust attenuation from the DAP

The MaNGA FIREFLY VAC is built upon the DAP. One of the advantages of that is that both provide data products for identical spectra from identical spatial bins. For that reason, spatially resolved parameters can be directly compared to each other.

The following figures can be understood as kind of sanity checks and as explorations of the general distributions of parameters in the catalogues rather than deep scientific analyses, which would
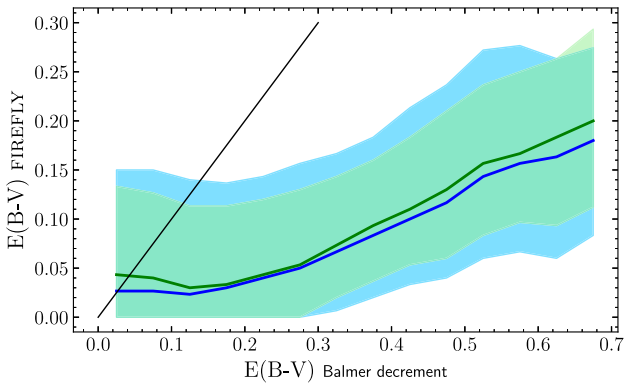
Figure 16. Comparison of colour excess measured from stellar population fitting (FIREFLY) and emission-line analysis (DAP). The black line shows the one-to-one relation.

require more careful sample selections, adjustments and appropriate in-depths discussions.

In the first two columns of Fig. 15, we plot FIREFLY derived stellar ages against two commonly used age indicators (Poggianti & Barbaro 1997; Worthey & Ottaviani 1997; Bruzual & Charlot 2003; Kauffmann et al. 2003) as measured by the DAP: the equivalent width of the Balmer absorption line Hδ and the 4000-Å break index D$_n$(4000) (Balogh et al. 1999). This analysis is again based on single spatial bins of the 300 galaxy subsample described previously. We see that age anticorrelates with Hδ and correlates with D$_n$(4000). The correlation with light-weighted ages is steeper and stronger than with mass-weighted ages (Spearman's rank $\rho = 0.70$ and 0.55 for Hδ; $\rho = 0.68$ and 0.53 for D$_n$(4000)). This confirms expectations, because both indices are most sensible to stellar ages below 2 Gyr (e.g. Bruzual & Charlot 2003) and changes in the young stellar populations dominate light-weighted ages more strongly. Maraston (2005) pointed out that D$_n$(4000) is not a pure age indicator but also sensible to changes in metallicity. To test this, we plot the same relation between age and both indices binned in four metallicity ranges. In agreement with Maraston (2005), at a given age, different Hδ and D$_n$(4000) are found for varying metallicity. The most metal-poor populations correspond to the lowest values of Hδ and the highest values of D$_n$(4000). Care should be taken when using them as pure age indicator.

Fig. 16 presents a comparison between the colour excess $E(B - V)$, on the one hand, derived as part of the full spectral stellar population fitting process by FIREFLY and, on the other hand, derived from the emission-line measurements in the DAP using the reddening of the Balmer decrement and assuming a Case B recombination $E(B - V) = 1.97 \log_{10} [(H\alpha/H\beta)/2.86]$ (Baker & Menzel 1938; Osterbrock 1989). Despite the fact that both colour excesses are measured in two completely different and independent ways, we find a clear positive correlation, yet with a large amount of scatter. Furthermore, the FIREFLY values are clearly below the one-to-one correlation for both variants of the VAC. The reddening from the Balmer decrement is expected to be higher because it captures the close, dusty environment of young stellar populations.

7 SUMMARY

We have presented the DR17 MaNGA FIREFLY VAC in its two variants FF-Mi and FF-Ma; a catalogue of spatially resolved stellar population properties of 10 010 nearby galaxies from the

MaNGA survey, obtained through state-of-the-art full spectral fitting of data with stellar population models. Both variants are structurally identical catalogues of the same sample, once fitted with M11-MILES and once with the MaStar stellar population models, respectively. Parameters provided in the VAC include stellar ages, metallicities, stellar and remnant masses, star formation histories, and dust attenuation; a full list of the content can be found in Table A1. The VAC is a major update to earlier data release versions (Goddard et al. 2017) and this paper is the first complete description of the VAC. It contains updates to the FIREFLY (Wilkinson et al. 2017) code itself as well as further elements of the parameter estimation and VAC construction.

A schematic illustration of the workflow can be found in Fig. 3, example fits in Figs 4 and 5 and a comparison of the distribution of stellar population properties in Fig. 6.

The major new additions of this VAC is the inclusion of the FF-Ma variant employing the novel MaStar models (Maraston et al. 2020, Maraston et al., in preparation) based on the MaStar stellar library (Yan et al. 2019) observed with the same instrument over the same wavelength range as the MaNGA data. The same MaStar models are also used as input for the data analysis pipeline (Westfall et al. 2019). Owing to the large sample size in MaStar the parameter space is much better sampled allowing for an extended model grid including low-age, low-metallicity templates.

We perform a variety of fitting tests and comparisons with different configurations in order to aid understanding the fitted stellar population parameters included in this VAC. FF-Ma provides on average slightly younger ages, higher mass-weighted metallicities and smaller colour excesses than FF-Mi. These differences are reduced when matching the wavelengths range and model parameter grid. We further provide a comparison between the FIREFLY VAC and other MaNGA stellar population catalogues. The masses in the MaNGA FIREFLY VAC are systematically lower by ~ 0.3 dex, but match the photometrically derived masses in the NSA catalogue best.

This version of the VAC has been published as an official VAC together with DR17 of SDSS. Performance tests (Section 5) and the calculation of SFRs (Section 3.4.4 and 6.3) have been performed after the official release. Furthermore, we foresee to update the catalogue with new variants employing later versions of the MaStar model library and we are also looking into using variable IMFs as a free parameter in the fitting procedure in future versions. SFRs and updates to the DR17 VAC will be published on the ICG Portsmouth institute's website: http://www.icg.port.ac.uk/manga-firefly-vac.

ACKNOWLEDGEMENTS

support and resources from the Center for High-Performance Computing at the University of Utah. The SDSS website is www.sdss.org.

SDSS is managed by the Astrophysical Research Consortium for the Participating Institutions of the SDSS Collaboration including the Brazilian Participation Group, the Carnegie Institution for Science, Carnegie Mellon University, the Chilean Participation Group, the French Participation Group, Harvard-Smithsonian Centre for Astrophysics, Instituto de Astrofísica de Canarias, The Johns Hopkins University, Kavli Institute for the Physics and Mathematics of the Universe (IPMU)/University of Tokyo, the Korean Participation Group, Lawrence Berkeley National Laboratory, Leibniz Institut für Astrophysik Potsdam (AIP), Max-Planck-Institut für Astronomie (MPIA Heidelberg), Max-Planck-Institut für Astrophysik (MPA Garching), Max-Planck-Institut für Extraterrestrische Physik (MPE), National Astronomical Observatories of China, New Mexico State University, New York University, University of Notre Dame, Observatório Nacional/MCTI, The Ohio State University, Pennsylvania State University, Shanghai Astronomical Observatory, United Kingdom Participation Group, Universidad Nacional Autónoma de México, University of Arizona, University of Colorado Boulder, University of Oxford, University of Portsmouth, University of Utah, University of Virginia, University of Washington, University of Wisconsin, Vanderbilt University, and Yale University.

DATA AVAILABILITY

The MaNGA FIREFLY VAC described in this paper can be downloaded from the SDSS website https://www.sdss.org/dr17/manga/manga-data/manga-firefly-value-added-catalog or from the ICG Portsmouth's website http://www.icg.port.ac.uk/manga-firefly-vac. It is also available as CAS table on the SDSS skyserver (http://skyserver.sdss.org/dr17) and integrated in MARVIN (https://dr17.sdss.org/marvin). The FIREFLY code is publicly available at https://github.com/FireflySpectra/firefly_release and is described at https://www.icg.port.ac.uk/firefly and https://www.sdss.org/dr17/spectro/galaxy_firefly. The stellar population models used in this paper are available at https://svn.sdss.org/public/data/sdss/stellarpopmodels/tags/v1_0_2/ and http://www.icg.port.ac.uk/mastar and also integrated in the FIREFLY GITHUB package.

REFERENCES

Abdurro'uf et al., 2021, ApJS, 259, 39
Aguado D. S. et al., 2019, ApJS, 240, 23
Baker J. G., Menzel D. H., 1938, ApJ, 88, 52
Balogh M. L., Morris S. L., Yee H. K. C., Carlberg R. G., Ellingson E., 1999, ApJ, 527, 54
Beifiori A., Maraston C., Thomas D., Johansson J., 2011, A&A, 531, A109
Belfiore F. et al., 2017, MNRAS, 469, 151
Belfiore F. et al., 2019, AJ, 158, 160
Bittner A. et al., 2019, A&A, 628, A117
Blanton M. R. et al., 2017, AJ, 154, 28
Blanton M. R., Kazin E., Muna D., Weaver B. A., Price-Whelan A., 2011, AJ, 142, 31
Brinchmann J., Charlot S., White S. D. M., Tremonti C., Kauffmann G., Heckman T., Brinkmann J., 2004, MNRAS, 351, 1151
Bruzual A. G., Charlot S., 1993, ApJ, 405, 538
Bruzual G., Charlot S., 2003, MNRAS, 344, 1000
Bryant J. J. et al., 2015, MNRAS, 447, 2857
Bundy K. et al., 2015, ApJ, 798, 7
Calzetti D., Armus L., Bohlin R. C., Kinney A. L., Koornneef J., Storchi-Bergmann T., 2000, ApJ, 533, 682
Cappellari M. et al., 2011, MNRAS, 413, 813
Cappellari M., 2017, MNRAS, 466, 798

Cappellari M., Copin Y., 2003, MNRAS, 342, 345
Cappellari M., Emsellem E., 2004, PASP, 116, 138
Carnall A. C., McLure R. J., Dunlop J. S., Davé R., 2018, MNRAS, 480, 4379
Cassisi S., Castellani M., Castellani V., 1997, A&A, 317, 108
Chen Y.-P. et al., 2020, ApJ, 899, 62
Cherinka B. et al., 2019, AJ, 158, 74
Chevallard J., Charlot S., 2016, MNRAS, 462, 1415
Cid Fernandes R., Mateus A., Sodré L., Stasińska G., Gomes J. M., 2005, MNRAS, 358, 363
Comparat J. et al., 2017, A&A, preprint (arXiv:1711.06575)
Conroy C., Gunn J. E., White M., 2009, ApJ, 699, 486
Conroy C., Villaume A., van Dokkum P. G., Lind K., 2018, ApJ, 854, 139
Croom S. M. et al., 2012, MNRAS, 421, 872
Dawson K. S. et al., 2013, AJ, 145, 10
de Zeeuw P. T. et al., 2002, MNRAS, 329, 513
Domínguez Sánchez H., Bernardi M., Brownstein J. R., Drory N., Sheth R. K., 2019, MNRAS, 489, 5612
Drory N. et al., 2015, AJ, 149, 77
Eisenstein D. J. et al., 2011, AJ, 142, 72
Falcón-Barroso J. et al., 2006, MNRAS, 369, 529
Falcón-Barroso J., Sánchez-Blázquez P., Vazdekis A., Ricciardelli E., Cardiel N., Cenarro A. J., Gorgas J., Peletier R. F., 2011, A&A, 532, A95
Fioc M., Rocca-Volmerange B., 1997, A&A, 500, 507
Fitzpatrick E. L., 1999, PASP, 111, 63
Goddard D. et al., 2017, MNRAS, 466, 4731
Gomes J. M., Papaderos P., 2017, A&A, 603, A63
González Delgado R. M. et al., 2015, A&A, 581, A103
Gunn J. E. et al., 2006, AJ, 131, 2332
Hill L. et al., 2022, MNRAS, 509, 4308
Ho I. T. et al., 2016, Ap&SS, 361, 280
Husemann B., Bennert V. N., Scharwächter J., Woo J.-H., Choudhury O. S., 2016, MNRAS, 455, 1905
Imig J. et al., 2022, AJ, 163, 18
Johnson B. D., Leja J., Conroy C., Speagle J. S., 2021, ApJS, 254, 22
Kauffmann G. et al., 2003, MNRAS, 346, 1055
Kennicutt R. C. Jr., 1998, ARA&A, 36, 189
Koleva M., Prugniel P., Bouchard A., Wu Y., 2009, A&A, 501, 1269
Kroupa P., 2001, MNRAS, 322, 231
Lacerda E. A. D., Sánchez S. F., Mejía-Narváez A., Camps-Fariña A., Espinosa-Ponce C., Barrera-Ballesteros J. K., Ibarra-Medel H., Lugo-Aranda A. Z., 2022, preprint (arXiv:2202.08027)
Lacerna I., Ibarra-Medel H., Avila-Reese V., Hernández-Toledo H. M., Vázquez-Mata J. A., Sánchez S. F., 2020, A&A, 644, A117
Law D. R. et al., 2015, AJ, 150, 19
Law D. R. et al., 2016, AJ, 152, 83
Law D. R. et al., 2021, AJ, 161, 52
Leitherer C. et al., 1999, ApJS, 123, 3
Lian J. et al., 2018, MNRAS, 476, 3883
Madau P., Dickinson M., 2014, ARA&A, 52, 415
Maraston C. et al., 2020, MNRAS, 496, 2962
Maraston C., 1998, MNRAS, 300, 872
Maraston C., 2005, MNRAS, 362, 799
Maraston C., Strömbäck G., 2011, MNRAS, 418, 2785
Maraston C., Strömbäck G., Thomas D., Wake D. A., Nichol R. C., 2009, MNRAS, 394, L107
Marigo P., Girardi L., Bressan A., Groenewegen M. A. T., Silva L., Granato G. L., 2008, A&A, 482, 883
Neumann J. et al., 2020, A&A, 637, A56
Neumann J. et al., 2021, MNRAS, 508, 4844
Ocvirk P., Pichon C., Lançon A., Thiébaut E., 2006a, MNRAS, 365, 46
Ocvirk P., Pichon C., Lançon A., Thiébaut E., 2006b, MNRAS, 365, 74
Osterbrock D. E., 1989, Astrophysics of Gaseous Nebulae and Active Galactic Nuclei. University Science Books, Melville, NY
Oyarzún G. A. et al., 2019, ApJ, 880, 111
Pace Z. J. et al., 2019a, ApJ, 883, 82
Pace Z. J. et al., 2019b, ApJ, 883, 83
Parikh T. et al., 2018, MNRAS, 477, 3954

Peng Y.-j. et al., 2010, ApJ, 721, 193
Pforr J., Maraston C., Tonini C., 2012, MNRAS, 422, 3285
Planck Collaboration XIII, 2016, A&A, 594, A13
Poetrodjojo H. et al., 2018, MNRAS, 479, 5235
Poggianti B. M., Barbaro G., 1997, A&A, 325, 1025
Renzini A., Ciotti L., 1993, ApJ, 416, L49
Renzini A., Peng Y.-J., 2015, ApJ, 801, L29
Rodríguez-Merino L. H., Chavez M., Bertone E., Buzzoni A., 2005, ApJ, 626, 411
Salpeter E. E., 1955, ApJ, 121, 161
Sánchez S. F. et al., 2012, A&A, 538, A8
Sánchez S. F. et al., 2016a, RMxAA, 52, 21
Sánchez S. F. et al., 2016b, A&A, 594, A36
Sánchez S. F. et al., 2018, Rev. Mex. Astron. Astrofis., 54, 217
Sánchez-Blázquez P. et al., 2006, MNRAS, 371, 703
Sánchez-Blázquez P. et al., 2014, A&A, 570, A6
Sarzi M. et al., 2006, MNRAS, 366, 1151
Schaller G., Schaerer D., Meynet G., Maeder A., 1992, A&AS, 96, 269
Schlegel D. J., Finkbeiner D. P., Davis M., 1998, ApJ, 500, 525
Smee S. A. et al., 2013, AJ, 146, 32
Thomas D., Maraston C., Schawinski K., Sarzi M., Silk J., 2010, MNRAS, 404, 1775
Tojeiro R., Heavens A. F., Jimenez R., Panter B., 2007, MNRAS, 381, 1252
Trussler J., Maiolino R., Maraston C., Peng Y., Thomas D., Goddard D., Lian J., 2020, MNRAS, 491, 5406

Vazdekis A., Casuso E., Peletier R. F., Beckman J. E., 1996, ApJS, 106, 307
Vazdekis A., Koleva M., Ricciardelli E., Röck B., Falcón-Barroso J., 2016, MNRAS, 463, 3409
Vazdekis A., Sánchez-Blázquez P., Falcón-Barroso J., Cenarro A. J., Beasley M. A., Cardiel N., Gorgas J., Peletier R. F., 2010, MNRAS, 404, 1639
Wake D. A. et al., 2017, AJ, 154, 86
Walcher C. J., Coelho P. R. T., Gallazzi A., Bruzual G., Charlot S., Chiappini C., 2015, A&A, 582, A46
Walcher C. J., Coelho P., Gallazzi A., Charlot S., 2009, MNRAS, 398, L44
Westfall K. B. et al., 2019, AJ, 158, 231
Wilkinson D. M., Maraston C., Goddard D., Thomas D., Parikh T., 2017, MNRAS, 472, 4297
Wisnioski E. et al., 2015, ApJ, 799, 209
Worthey G., 1994, ApJS, 95, 107
Worthey G., Ottaviani D. L., 1997, ApJS, 111, 377
Yan R. et al., 2016a, AJ, 151, 8
Yan R. et al., 2016b, AJ, 152, 197
Yan R. et al., 2019, ApJ, 883, 175

APPENDIX A: VAC CONTENT

Here we present the content of the MaNGA FIREFLY VAC in Table A1.

Table A1. MaNGA FIREFLY VAC – content of catalogue.

HDU (1)	Name (2)	Dimensions (3)	Units (4)	Description (5)
0	PRIMARY			Empty primary header.
1	MANGAID			Unique MaNGA identifier.
	PLATEIFU			Unique identifier containing the MaNGA plate and ifu combination.
	PLATE			Plate used to observe galaxy.
	IFUDSGN			IFU used to observe galaxy.
	OBJRA			Right ascension of the galaxy, not the IFU.
	OBJDEC			Declination of the galaxy, not the IFU.
	REDSHIFT			Redshift of the galaxy.
	PHOTOMETRIC_MASS		$\log_{10}$ ($M_\odot$)	Stellar mass of galaxy from NSA catalogue obtained from K-correction fits to elliptical Petrosian photometric fluxes. Masses are converted to the cosmology parameters that we assume in the FIREFLY VAC with $H_0 = 67.8 \, \mathrm{km \, s^{-1} \, Mpc^{-1}}$
	MANGADRP_VER			Version of MaNGA DRP that produced these data.
	MANGADAP_VER			Version of MaNGA DAP that analysed these data.
	FIREFLY_VER			Version of FIREFLY that analysed these data.
2	LW_AGE_1Re		$\log_{10}$ ($M_\odot$)	Light-weighted age within a shell located at $1R_e$.
	LW_AGE_1Re_ERROR		$\log_{10}$ ($M_\odot$)	Error on light-weighted age within a shell located at $1R_e$.
	MW_AGE_1Re		$\log_{10}$ ($M_\odot$)	Mass-weighted age within a shell located at $1R_e$.
	MW_AGE_1Re_ERROR		$\log_{10}$ ($M_\odot$)	Error on mass-weighted age within a shell located at $1R_e$.
	LW_Z_1Re			Light-weighted metallicity [Z/H] within a shell located at $1R_e$.
	LW_Z_1Re_ERROR			Error on light-weighted metallicity [Z/H] within a shell located at $1R_e$.
	MW_Z_1Re			Mass-weighted metallicity [Z/H] within a shell located at $1R_e$.
	MW_Z_1Re_ERROR			Error on mass-weighted metallicity [Z/H] within a shell located at $1R_e$.
	LW_AGE_3ARCSEC		$\log_{10}$ ($M_\odot$)	Light-weighted age within 3-arcsec diameter.
	LW_AGE_3ARCSEC_ERROR		$\log_{10}$ ($M_\odot$)	Error on light-weighted age within 3 arcsec.
	MW_AGE_3ARCSEC		$\log_{10}$ ($M_\odot$)	Mass-weighted age within 3-arcsec diameter.
	MW_AGE_3ARCSEC_ERROR		$\log_{10}$ ($M_\odot$)	Error on mass-weighted age within 3 arcsec.
	LW_Z_3ARCSEC			Light-weighted metallicity [Z/H] within 3-arcsec diameter.
	LW_Z_3ARCSEC_ERROR			Error on light-weighted metallicity [Z/H] within 3 arcsec.
	MW_Z_3ARCSEC			Mass-weighted metallicity [Z/H] within 3-arcsec diameter.
	MW_Z_3ARCSEC_ERROR			Error on mass-weighted metallicity [Z/H] within 3 arcsec.
3	LW_AGE_GRADIENT		dex/R_e	Light-weighted age gradient of linear fit obtained within $1.5R_e$.
	LW_AGE_GRADIENT_ERROR		dex/R_e	Error on light-weighted age gradient within $1.5R_e$.
	LW_AGE_ZEROPOINT			Light-weighted age zero-point of linear fit obtained within $1.5R_e$.
	LW_AGE_ZEROPOINT_ERROR			Error on light-weighted age zero-point obtained within $1.5R_e$.
	MW_AGE_GRADIENT		dex/R_e	Mass-weighted age gradient of linear fit obtained within $1.5R_e$.
	MW_AGE_GRADIENT_ERROR		dex/R_e	Error on mass-weighted age gradient within $1.5R_e$.
	MW_AGE_ZEROPOINT			Mass-weighted age zero-point of linear fit obtained within $1.5R_e$.
	MW_AGE_ZEROPOINT_ERROR			Error on mass-weighted age zero-point obtained within $1.5R_e$.
	LW_Z_GRADIENT		dex/R_e	Light-weighted metallicity [Z/H] gradient of linear fit obtained within $1.5R_e$.
	LW_Z_GRADIENT_ERROR		dex/R_e	Error on light-weighted metallicity [Z/H] gradient within $1.5R_e$.

Table A1 – *continued*

HDU (1)	Name (2)	Dimensions (3)	Units (4)	Description (5)
	LW_Z.ZEROPOINT			Light-weighted metallicity [Z/H] zero-point of linear fit obtained within $1.5R_e$.
	LW_Z.ZEROPOINT_ERROR			Error on light-weighted metallicity [Z/H] zero-point obtained within $1.5R_e$.
	MW_Z.GRADIENT		dex/R_e	Mass-weighted metallicity [Z/H] gradient of linear fit obtained within $1.5R_e$.
	MW_Z.GRADIENT_ERROR		dex/R_e	Error on mass-weighted metallicity [Z/H] gradient within $1.5R_e$.
	MW_Z.ZEROPOINT			Mass-weighted metallicity [Z/H] zero-point of linear fit obtained within $1.5R_e$.
	MW_Z.ZEROPOINT_ERROR			Error on mass-weighted metallicity [Z/H] zero-point obtained within $1.5R_e$.
4	SPATIAL INFORMATION (VORONOI CELL)	(5, 2800, 10 735)	N/A, arcsec, arcsec, R_e, deg	Spatial information, such as bin number, x-position, y-position and, in elliptical polar coordinates, radius (in units of effective radius) and azimuth for each Voronoi cell.
5	SPATIAL INFORMATION (SPAXEL)	(80, 80, 10 735)	N/A	2D map of bin number.
6	LIGHT-WEIGHTED AGE	(2, 2800, 10 735)	$\log_{10}$ (Gyr)	Light-weighted age, and associated error, derived from full spectral fit for each Voronoi cell.
7	MASS-WEIGHTED AGE	(2, 2800, 10 735)	$\log_{10}$ (Gyr)	Mass-weighted age, and associated error, derived from full spectral fit for each Voronoi cell.
8	LIGHT-WEIGHTED METALLICITY	(2, 2800, 10 735)	N/A	Light-weighted metallicity [Z/H], and associated error, derived from full spectral fit for each Voronoi cell.
9	MASS-WEIGHTED METALLICITY	(2, 2800, 10 735)	N/A	Mass-weighted metallicity [Z/H], and associated error, derived from full spectral fit for each Voronoi cell.
10	$E(B-V)$	(2800, 10 735)	mag	$E(B-V)$ derived from using high-pass filter (HPF) method for each Voronoi cell (see Goddard et al. 2017).
11	STELLAR MASS	(4, 2800, 10 735)	0–1: $\log_{10}(M_\odot/\text{spaxel})$ 2–3: $\log_{10}(M_\odot)$	Stellar mass, and associated error, derived from the full spectral fit for each Voronoi cell. Different to the global stellar mass. The first two channels give the stellar mass and error per spaxel, the last two channels give the total stellar mass and error of the Voronoi cell.
12	STELLAR MASS REMNANT	(8, 2800, 10 735)	0–3: $\log_{10}(M_\odot/\text{spaxel})$ 4–7: $\log_{10}(M_\odot)$	Mass of living stars, stellar remnants including white dwarf, neutron star, and black hole. The first four channels give the masses per spaxel, the last four channels give the total masses per Voronoi cell.
13	SURFACE MASS DENSITY	(2, 2800, 10 735)	$\log_{10}(M_\odot\ \text{kpc}^{-2})$	Surface mass density, and associated error, derived from the full spectral fit for each Voronoi cell.
14	STAR FORMATION HISTORY	(3, 8, 2800, 10 735)	$\log_{10}$ (Gyr), N/A, N/A	Star formation history in each Voronoi cell reflected by the mass weight of each SSP that contributes to the observed spectra. The first channel of the array includes the age, metallicity [Z/H], and mass weights of each of the eight SSPs given in the second channel.
15	SIGNAL-TO-NOISE	(2800, 10 735)	S/N	Signal-to-noise ratio calculated for each Voronoi cell in the wavelength range 4500–6000 Å.

APPENDIX B: DETAILS FROM FIREFLY CONFIGURATION TESTS

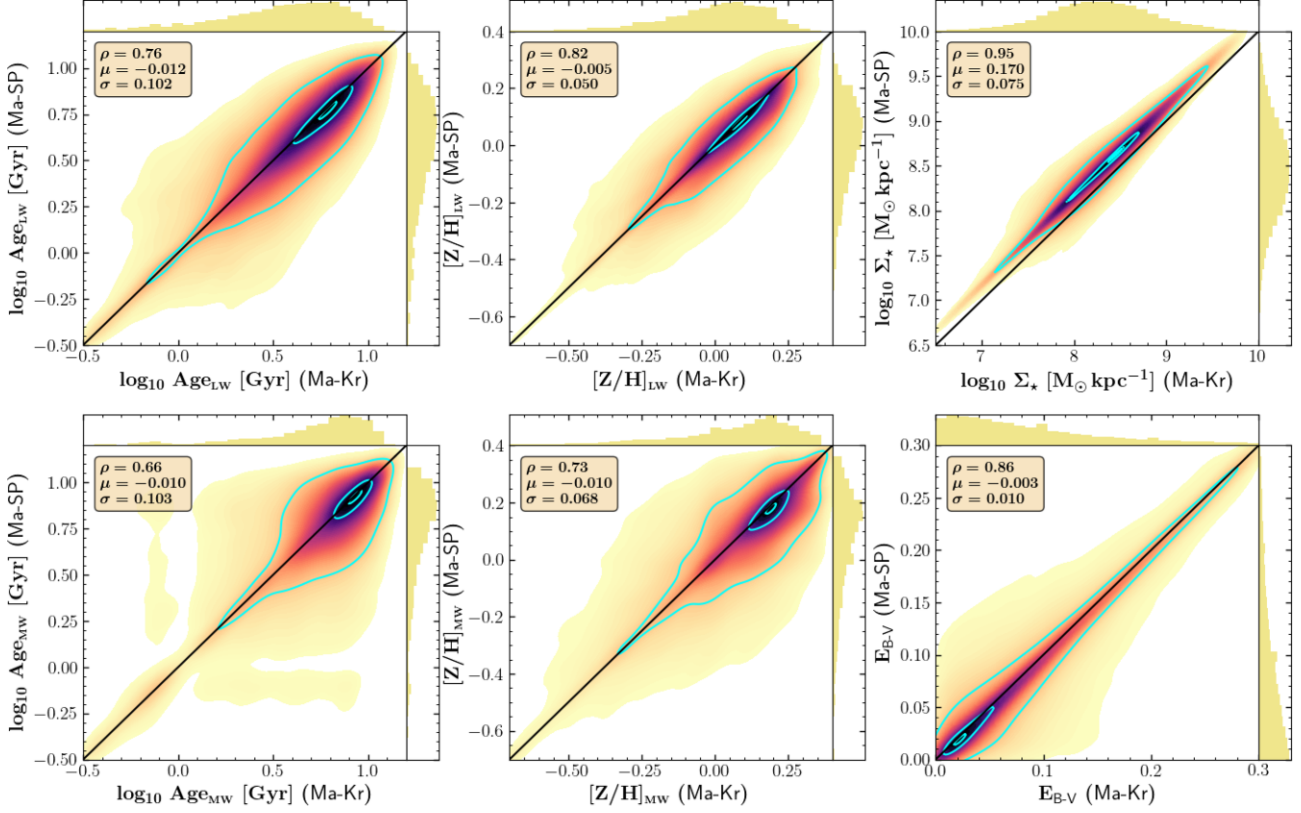We provide detailed plots from the configurations tests described in Section 4.3 in Figs B1–B7.

Figure B1. Same as Fig. 6 but comparing fits using MaStar SSPs with a Kroupa versus Salpeter IMF.
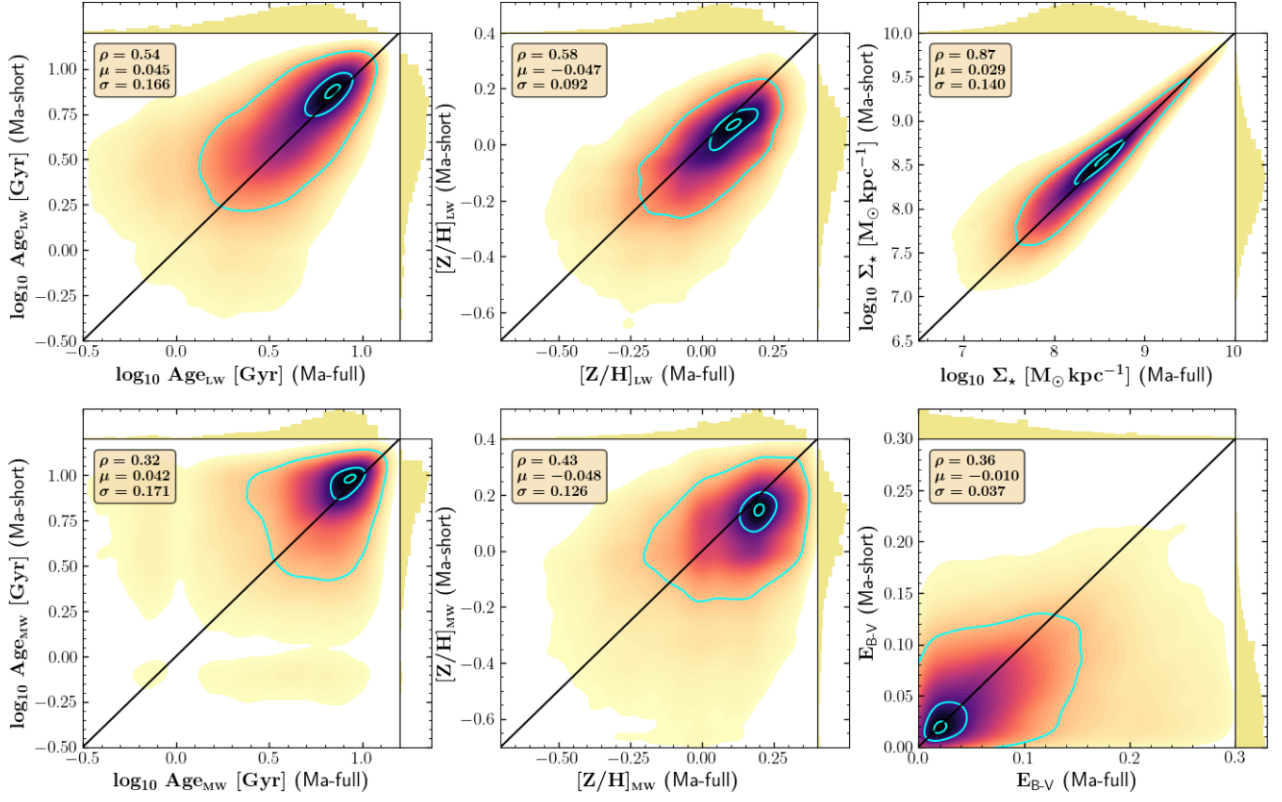
Figure B2. Same as Fig. 6 but comparing fits using Mastar with a full wavelength range versus MaStar with a short wavelength range.
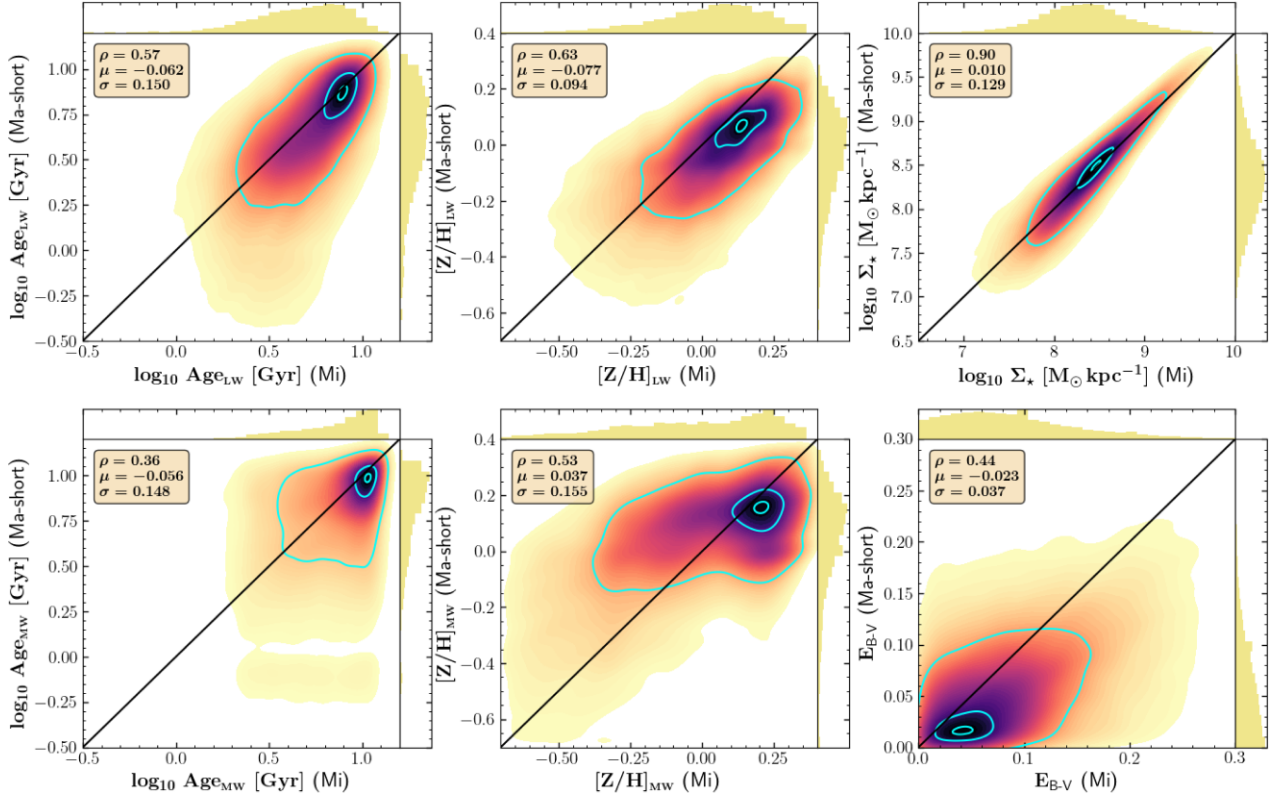
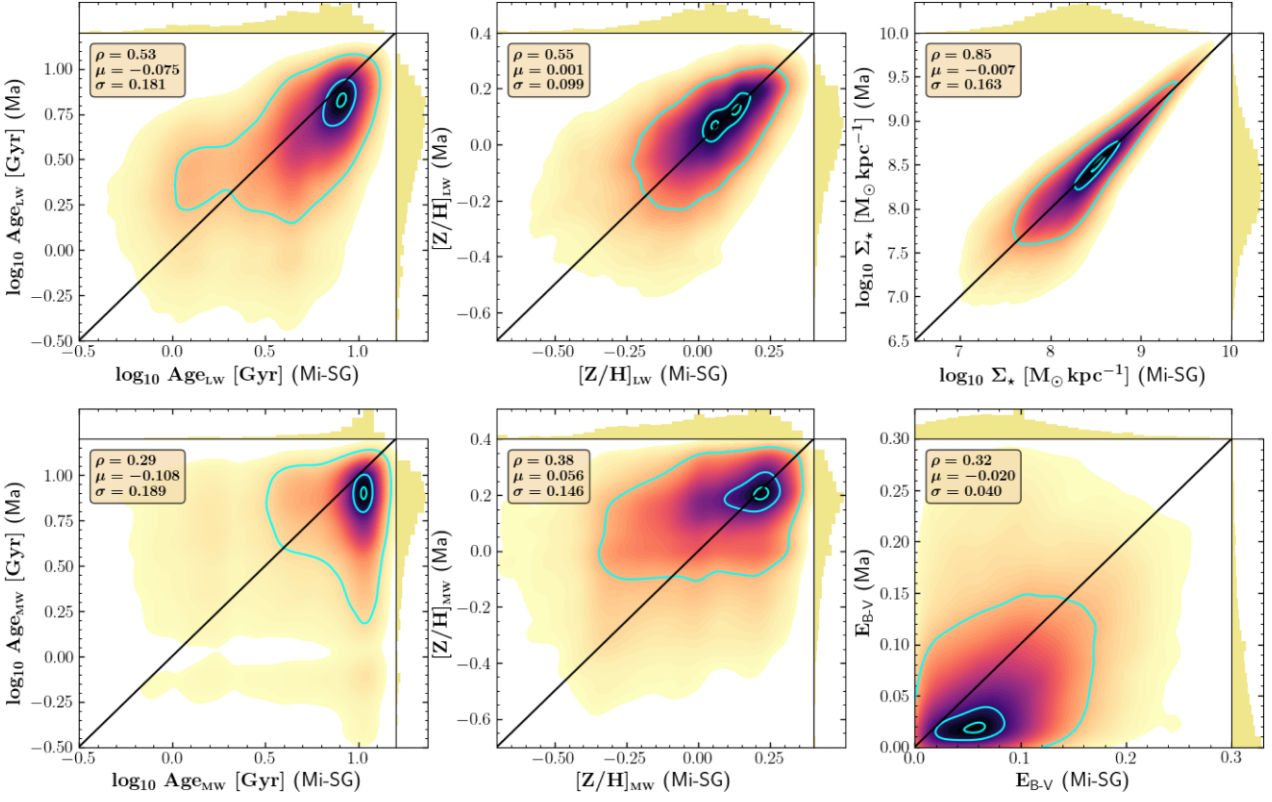**Figure B3.** Same as Fig. 6 but comparing fits using M11-MILES and MaStar with the same short wavelength range.

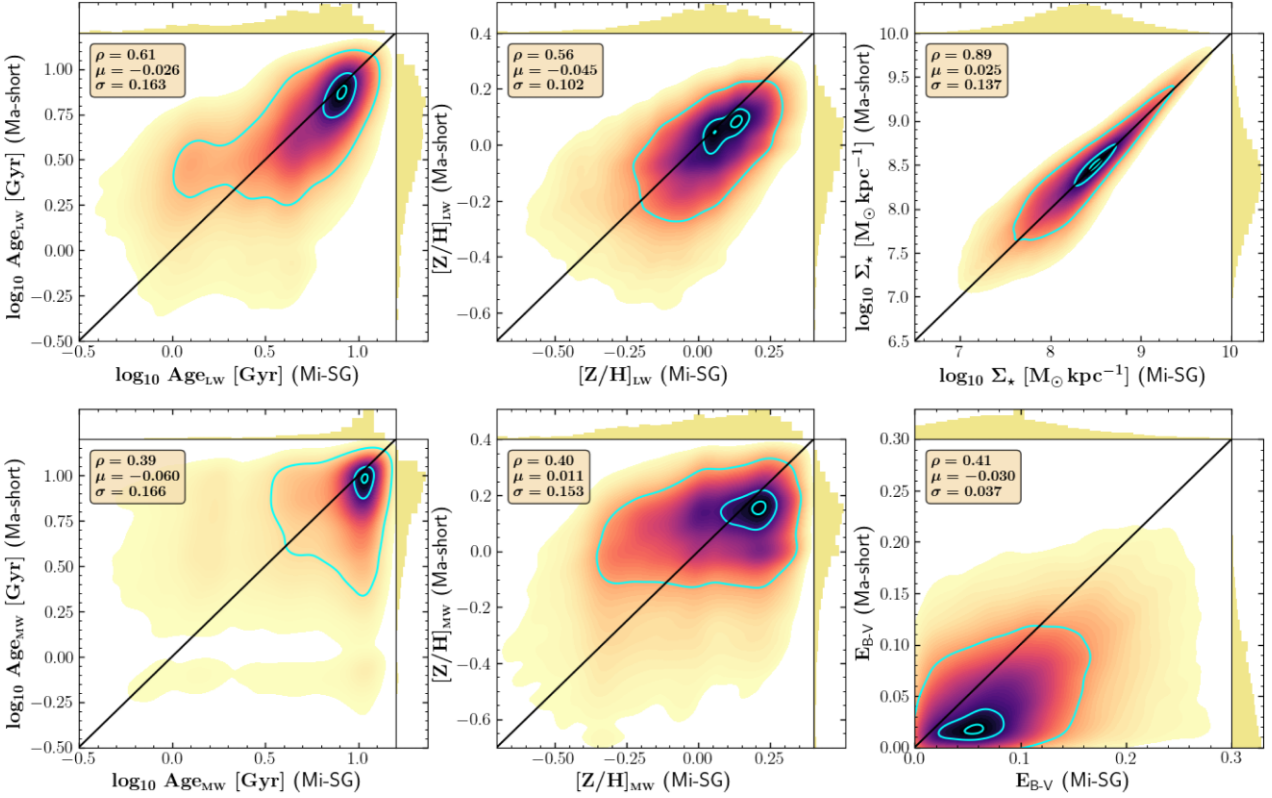**Figure B4.** Same as Fig. 6 but comparing fits using M11-MILES squared grid models versus MaStar models.

Figure B5. Same as Fig. 6 but comparing fits using M11-MILES squared grid models versus MaStar models with a short wavelength range.
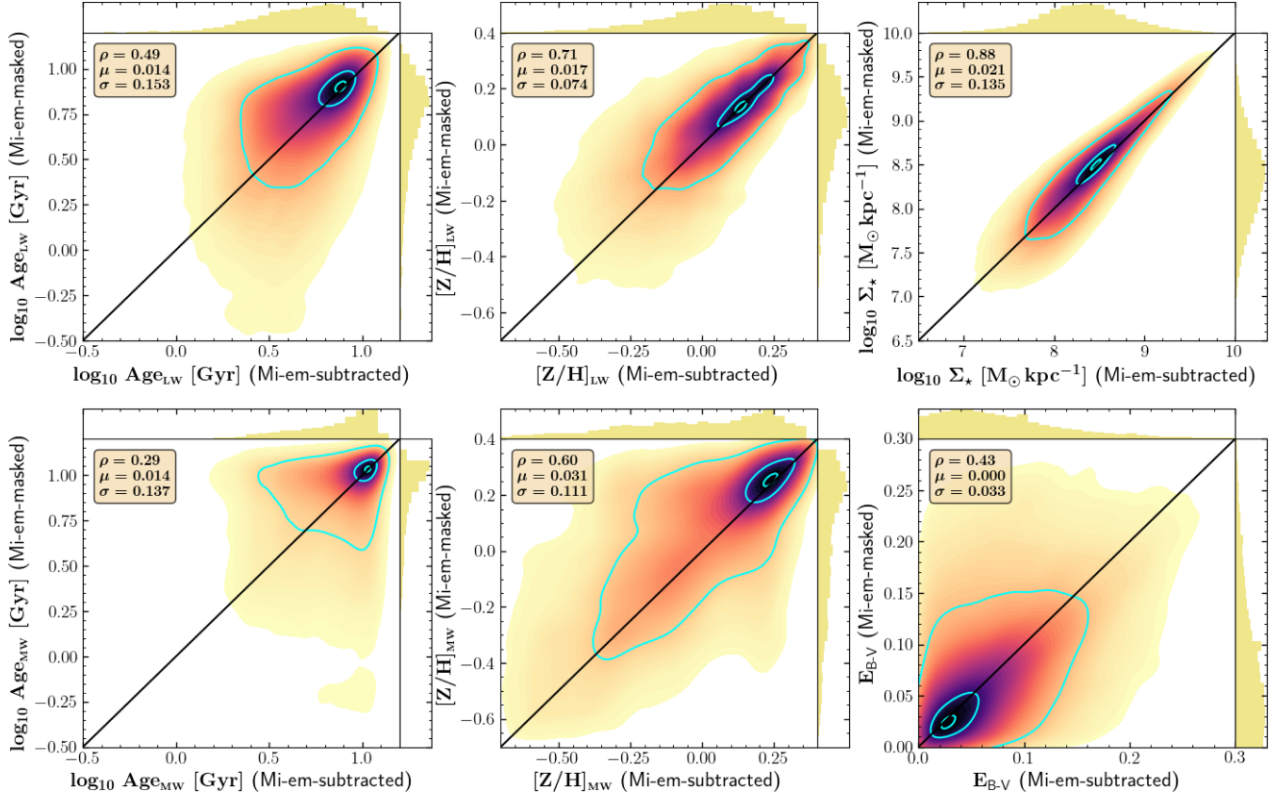
Figure B6. Same as Fig. 6 but comparing fits using M11-MILES models with emission-line-subtracted versus emission lines masked.
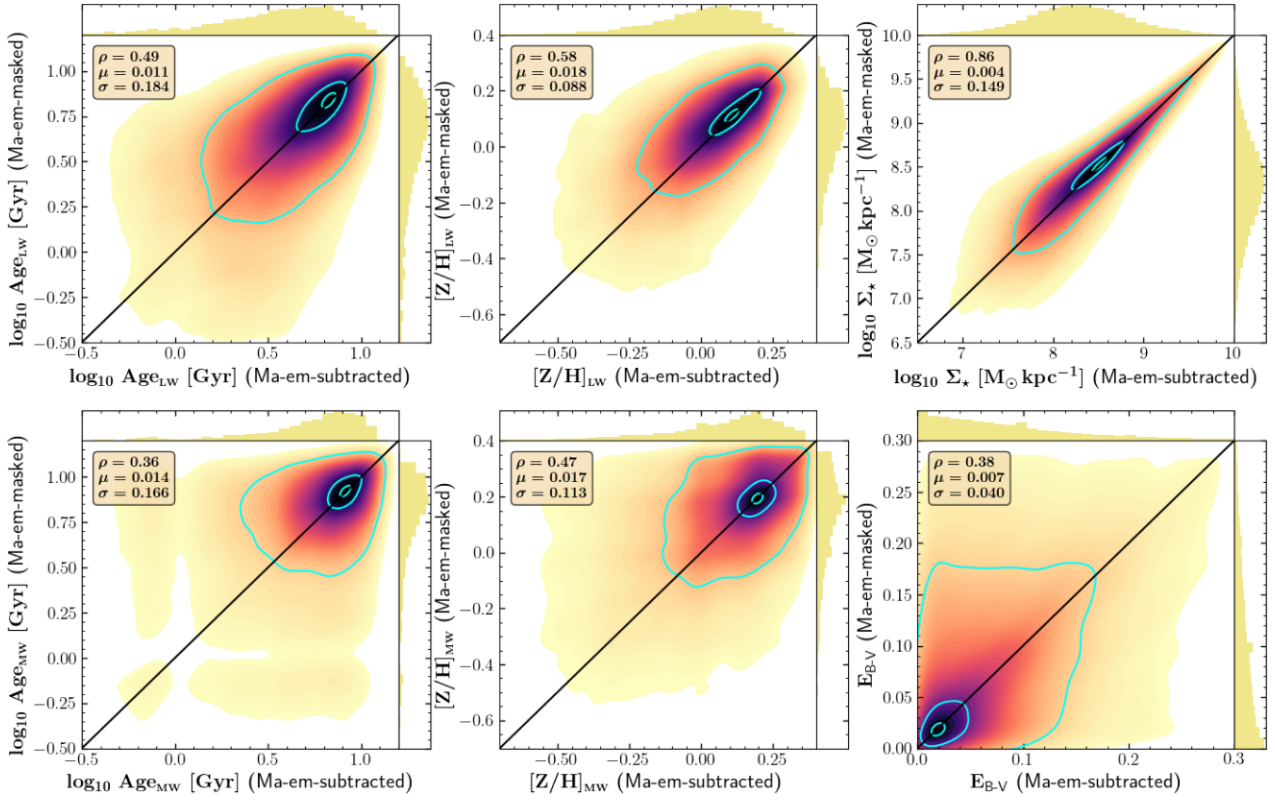
Figure B7. Same as Fig. 6 but comparing fits using Mastar models with emission-lines subtracted versus emission lines masked.

This paper has been typeset from a TEX/LATEX file prepared by the author.